# Fractionation of trace and platinum-group elements during metamorphism of komatiitic chromites from the early Archean Gorumahishani greenstone belt, Singhbhum Craton (eastern India)

Ratul Banerjee, Sisir K Mondal, Laurie Reisberg, Jung-Woo Park

## To cite this version:

Ratul Banerjee, Sisir K Mondal, Laurie Reisberg, Jung-Woo Park. Fractionation of trace and platinum-group elements during metamorphism of komatiitic chromites from the early Archean Gorumahishani greenstone belt, Singhbhum Craton (eastern India). Contributions to Mineralogy and Petrology, 2022, 177, 10.1007/s00410-022-01943-4 . hal-03864185

**HAL Id: hal-03864185**

**https://hal.univ-lorraine.fr/hal-03864185**

Submitted on 21 Nov 2022

# Fractionation of trace and platinum-group elements during metamorphism of komatiitic chromites from the early Archean Gorumahishani greenstone belt, Singhbhum Craton (eastern India)

**Ratul Banerjee[a], Sisir K. Mondal[a]*, Laurie Reisberg[b], Jung-Woo Park[c]**

[a] Department of Geological Sciences, Jadavpur University, 188, Raja S.C. Mullik Road, Kolkata-700032, India
[b] Centre de Recherches Pétrographiques et Géochimiques, UMR 7358 Université de Lorraine - CNRS, France
[c] School of Earth and Environmental Sciences, Seoul National University, Seoul, 08826, South Korea

*Corresponding Author:
eMail: smondal@amnh.org
Phone: 0091-33-24572730

## Abstract

It is well established that the major and minor element contents of chromites are subject to change during greenschist to amphibolite facies metamorphism. During upper amphibolite facies metamorphism, chromite can be completely converted to chrome magnetite. However, not all elements are affected to the same degree, the concentrations of +2 ions (e.g. Zn, Co, Mn) being particularly vulnerable to modification. The degree to which trace elements, particularly the platinum-group elements (PGE), are affected has not been closely examined. The compositions and textures of chromites from komatiites of the Gorumahishani greenstone belt of the Singhbhum Craton (India) have experienced a range of metamorphic conditions from greenschist to amphibolite facies, providing the opportunity to study the changes of trace and platinum-group element composition with metamorphic grade. Five types of altered chromites are identified from the komatiitic suite of rocks in the ~120 km long greenstone belt. The type-I chromites are non-porous and characterized by the least modified cores. These chromites are mostly present in the northern Maharajgunj-Tua Dungri section where rocks show metamorphism from greenschist to greenschist-amphibolite transition facies. The type-II and type-III chromites are porous and mostly found in the southern Kapili section of the greenstone belt where rocks show metamorphism up to the mid-amphibolite facies. Type-IV and type-V chromites are completely modified to ferritchromit and chrome magnetite, respectively and are present in the komatiitic rocks from the entire greenstone belt. The central cores of the type-I and type-II grains have relatively higher concentrations of mobile trace elements (e.g. Zn, Co, and Mn) with higher Mg# [Mg/(Mg+$Fe^{2+}$)], lower Cr# [Cr/(Cr+Al)] and lower $Fe^{3+}/R^{3+}$ ($R^{3+} = Fe^{3+}+Cr^{3+}+Al^{3+}$) ratios than their respective rims. Significantly higher concentrations of the immobile trace elements (e.g. Ti and V) in the cores of the type-II grains relative to their chrome magnetite rims from the Kapili section, and to the type-I varieties from other sections might be due to the metamorphism of the komatiitic rocks under higher grade conditions (amphibolite facies). *In situ* LA-ICPMS analysis for PGE reveal a relatively higher concentration of Ru and Rh in the rims of the type-I chromites than in the cores which is due to the diffusion of these elements from the normal spinel structure of the cores towards the bivalent octahedral sites of the inverse spinel structure of the chrome magnetite rims during metamorphic processes. The lower concentrations of Os, Ir, Ru, and Rh in the cores of the type-II chromites from the Kapili section might be related to the metamorphism of the rocks under higher grade conditions that facilitated the diffusion of these elements to associated sulfide or platinum-group mineral or alloy phases. The calculated partition coefficients of Sc, Ti, V, Mn, Ni, Ga, Os, Ir, Ru, and Rh from the least altered chromite cores assuming equilibrium with the parental komatiitic melt also suggest the variable effects of metamorphism when compared with global experimental and empirical values of the natural samples.

**Keywords: komatiite . chromite . PGE and trace element . fractionation . metamorphism . Singhbhum Craton**

## Introduction

Chromite is an early crystallizing oxide phase in komatiites from greenstone belts. The Cr# [Cr/(Cr+Al)], Ti, Al and V of chromites are used as petrogenetic indicators in massive chromitites (e.g. Irvine 1967; Roeder 1994; Stowe 1997; Mondal et al. 2006; Mukherjee et al 2010) and in volcanic rocks (Kamenetsky et al. 2001; Canil 2002; Nicklas et al. 2016). However in komatiitic rocks, chromites as well as the primary silicate phases are often strongly affected by hydrothermal alteration and metamorphism (e.g. Barnes 1998, 2000, 2006). Such processes have led to textural variability and chemical modification of chromite in many ultramafic-mafic rocks from widely varying geological settings (Evans and Frost 1975; Kimball 1990; Burkhard 1993; Proenza et al. 2004; González Jiménez et al. 2009, 2014; Mukherjee et al. 2015; Colás et al. 2019) although studies of komatiitic chromites are relatively scarce (e.g., Zhou and Kerrich 1992; Barnes 1998, 2000; Godel et al. 2013). Major and minor element studies of komatiitic chromites (Barnes 1998, 2000) show that at low metamorphic grades the core compositions may retain their primary magmatic character (other than FeO content) and can be used to understand the crystallization environment. Diverse opinions exist concerning the formation of the characteristic optical and chemical zoning of ferritchromit and chrome magnetite rims in chromites e.g. (a) Such rims may result from subsolidus elemental exchange with silicate minerals during prograde metamorphism (Evans and Frost 1975; Wylie et al. 1987; Burkhard 1993; Barnes 2000; González Jiménez et al. 2009; Merlini et al. 2009), (b) In ophiolitic chromitites these features may reflect retrograde metamorphism during cooling from the eclogite facies (e.g. Proenza et al. 2008; Gervilla et al. 2012; Colás et al. 2014). The trace element data obtained from LA-ICPMS studies of chromites have been particularly useful in developing a more precise understanding of how these zoned rims formed (e.g. Pagé and Barnes 2009; Mukherjee et al. 2015; Colás et al. 2017; Yu et al. 2019). Such *in situ* techniques have also been used to study trace and platinum-group element (PGE) partitioning between volcanic chromites and co-existing high-Mg silicate melt from a variety of geological settings (Locmelis et al. 2011; Pagé et al. 2012; Kamentsky et al. 2015; Pagé and Barnes 2016; Arguin et al. 2016; Park et al. 2012, 2017).

In Eastern India, the ~120 km-long Archean Gorumahishani greenstone belt of the Singhbhum Craton includes an entire komatiitic rock suite (lower dunite-peridotite adcumulate to upper komatiitic basalt) in the lower part of the supracrustal sequence. Accessory chromite, chrome magnetite, and magnetite with textural and compositional zoning are quite common in these rocks (e.g. Mondal et al. 2019a). In the current study, *in situ* major, minor, trace, and PGE data, coupled with petrographic observations, are used to characterize komatiitic chromites from this greenstone belt, and classify them into different types. The characteristic trace and PGE concentration patterns in the compositionally modified chromites, and the differences between chromite cores and rims, are explained in terms of magmatic versus subsolidus processes. Our study is the first to discuss post magmatic modification of PGE distribution in komatiitic chromites and to correlate the patterns with degree of metamorphism of the rocks. Furthermore, we calculate apparent trace element (Sc, Ti, V, Mn, Zn, Co, Ni, Ga) and PGE (Os, Ir, Ru, Rh) chromite-komatiite partition coefficients using mass balance calculations based on the data of less altered chromite cores (e.g. Pagé and Barnes 2009, 2016; Park et al. 2017). These data are compared with other experimental and natural partitioning values to better discriminate between magmatic and subsolidus processes. Our primary goal in this study is to look at PGE and other trace elements hosted by the chromite itself but not at platinum-group mineral microinclusions.

## Geological background

The geological background of the Singhbhum Craton is described more fully in **Appendix 1** (**Fig. 1a**). The Archean granitic-gneissic nucleus of the craton is surrounded by greenschist to amphibolite facies volcano-sedimentary rocks of the Iron Ore Group (IOG) supracrustals that are present in three greenstone belts (e.g. Mondal 2009; **Fig. 1a**). This study concerns the Gorumahishani-Badampahar greenstone belt (**Fig. 1b**) of the IOG supracrustals which also include the Noamundi-Jamda-Koira and Tomka-Daitari greenstone belts (**Fig. 1a**). Komatiites and komatiitic basalts are the main volcanic lithologies, and are intercalated with sedimentary sequences of phyllite, tuffaceous shale, banded hematite jasper with iron ore, quartzites, and dolomite (Sahu and Mukherjee 2001; Chaudhuri et al. 2015, 2017; Yadav et al. 2015, 2017). U-Pb zircon ages of 3.5 and 3.4 Ga were determined respectively from dacite of the Tomka-Daitari belt (Mukhopadhyay et al., 2008) and a tuff layer within the Noamundi-Jamda-Koira belt (Basu et al., 2008), whereas a whole rock Sm-Nd isochron age of ~3.6 Ga (Adhikari et al., 2021) was obtained from metabasalts and komatiites of the Tomka-Daitari belt. The Gorumahishani schist belt follows an overall NW-SE trend, traceable from south of Tatanagar (Jharkhand state) in the north to Badampahar (Orissa state) in the south (**Fig. 1b**). The lower part of the greenstone sequence is composed of metamorphosed ultramafic-mafic extrusive rocks while the upper part comprises volcanogenic sediments and banded iron formation. Three parts of the belt, namely Maharajgunj-Chuka Pahar and Tua Dungri in the north and Kapili in the south (**Fig. 1b-e**) have been sampled and the rock types vary from dunite-peridotite (**Fig. 2a**) to spinifex-textured komatiite (**Fig. 2b-d**) to komatiitic basalt (**Fig. 2e**). In the Maharajgunj-Chuka Pahar and Tua Dungri sections, the dunite (~70 m) and the spinifex-textured komatiites (~100 m) are well exposed and thicker than in the Kapili sector.

## Petrography

### Dunite-peridotite cumulates (meta-dunite and meta-peridotite)

Metamorphosed dunite-peridotites are present in the lower part of the komatiite sequences (cumulate zone; **Fig. 2a**). Modal abundances of mineral phases (**Figs. 3, 4**) in meta-dunite and meta-peridotite from the Maharajgunj-Chuka Pahar and Tua Dungri sectors include, in decreasing order, serpentine, carbonates, tremolite, chlorite, and talc (**Fig. 4**). In the Kapili sector, the decreasing order of mineral abundances changes to serpentine, tremolite, chlorite, hornblende, and carbonate (**Figs. 3, 4**). A few micrometer-sized olivine grains are observed in samples from the Kapili area (**Fig. 3a**). Interstitial spaces between serpentines (pseudomorphic after olivine) are occupied by chlorite, tremolite, hornblende, talc, and carbonates (**Fig. 3b, c**). Chromites are present as an accessory phase in the metamorphosed dunite-peridotite (**Figs. 3, 4**). Sulfide minerals include pentlandite, millerite, cobalt-rich violarite, chalcopyrite, and bornite and occur in disseminated form at low modal abundances (Banerjee et al. 2021).

### Spinifex-textured komatiites (meta-peridotite)

The metamorphosed komatiitic peridotites from the spinifex zone show platy, random, and/or chevron spinifex textures (**Fig. 2b, d**). The spinifexes (~0.5 - 40 cm in length, and ~2 - 5 mm in width) are marked by deep cavities on the weathered surfaces of the rocks. Microscopic study reveals that in the Maharajgunj-Chuka Pahar and Tua Dungri sections, the modal abundances of serpentine are lower while modes of tremolite and chlorite are higher in the spinifex zone relative to the cumulate zone (**Figs. 3d, 4**). Tremolite, chlorite, hornblende and carbonate are the major minerals in the meta-peridotites of the spinifex zone from the Kapili section (**Figs. 3e, 4**). The primary minerals in spinifex laths are replaced by tremolite in Kapili, and to a lesser extent by serpentine in Tua Dungri (**Fig. 3d, e**). Chromites are present as an accessory phase in the meta-peridotites (**Figs. 3, 4**). Sulfide minerals are pentlandite, millerite, and cobalt-rich violarite which occur in the spinifex zone in very low modal abundances and show a similar petrographic character to the sulfides observed in the cumulate zone (Banerjee et al. 2021).

### Meta-basalts

The komatiitic basalts are altered to meta-basalts and show schistose character (**Fig. 2e**). In places, meta-basalts are interlayered with quartzites, indicating the top part of the komatiitic litho-package (e.g. Arndt et al. 2008). The meta-basalts have higher modal abundances of tremolite, chlorite, and actinolite in the Tua Dungri and Chuka Pahar sections, whereas hornblende is more abundant in the Kapili section (**Figs. 3f, 4**). Oxide mineralogy in the meta-basalts are represented by variable modes of fine-grained, anhedral chrome magnetite, magnetite and ilmenite (**Fig. 3h**).

### Textural types of chromites in komatiitic rocks

Chromite is present ubiquitously as an accessory mineral throughout the cumulate and spinifex zones of the Gorumahishani komatiite sequences (**Figs. 3, 4**). Microscopic study and back-scattered electron (BSE) imaging show that a few chromite grains are compositionally zoned with different textures and variable reflectance (**Fig. 5**). The zoned grains typically have a chromite core with a ferritchromit inner rim and chrome magnetite to magnetite outer rim (**Fig. 5a, b**). However, multiple inner rims of different reflectance and composition between chromite core and outer chrome magnetite rim are also observed (**Fig. 5c**). Ilmenite grains are present along the outermost margin of some zoned chromites (**Fig. 5b, c**). Based on petrographic observations and mineral chemistry the chromite grains are classified into five broad types (**Table 1**). Type-I chromites in the meta-dunite-peridotite of the cumulate zone from the Tua Dungri area, and type-II, type-III chromites in the meta-peridotite of the spinifex zone from the Kapili area are optically and texturally inhomogeneous (**Fig. 5**). In contrast, type-IV chromites in the meta-peridotite from the Maharajgunj area and type-V chromites in the komatiitic sequences from all locations are texturally homogeneous (**Fig. 3g, h**). Among the five types, type-V chromites have the highest modal abundance in komatiitic rocks, while the lowest modal abundance is displayed by the type-IV grains. The type-I and type-IV grains from the northern part of the greenstone belt are present in komatiitic rocks that were metamorphosed under greenschist to greenschist-amphibolite transition facies, whereas the type-II and type-III grains from the southern greenstone belt are present in komatiitic rocks that were metamorphosed under amphibolite facies. The type-V grains are present in the altered komatiitic rocks of all metamorphic grades throughout the greenstone belt.

## Analytical methods

Back-scattered electron (BSE) imaging and microanalysis of the mineral phases (oxides and silicates) of 8 representative samples were carried out using a CAMECA SXFive EPMA instrument at DST-SERB National Facility, Department of Geology, Banaras Hindu University (India). Another 14 samples were analyzed by 4-WDX CAMECA SX-100 EPMA at the Department of Geology and Geophysics, Indian Institute of Technology, Kharagpur (India). $Fe_2O_3$ and FeO concentrations of the silicate and oxide minerals were calculated following the equation of Droop (1987). Trace and platinum-group element concentrations in chromite, ferritchromit, and chrome magnetite were measured by laser ablation-inductively coupled plasma mass spectrometry (LA-ICPMS) at the Korea Institute of Ocean Sciences and Technologies, South Korea using an LA-ICPMS system consisting of a New Wave 193 nm ArF excimer laser and an Agilent 7800 quadrupole ICP-MS. Analyses of bulk-rock major, trace, and platinum-group elements, C and S for 2 representative komatiites were conducted by Intertek Genalysis, Perth, Western Australia. See **Appendix 1** for details of all the analytical methods.

## Results

### Silicate and carbonate mineral chemistry

All individual analyses of silicate and carbonate minerals are listed in **Appendix 3: Table S1**. The forsterite content of one tiny olivine found in the Kapili peridotite is 88 while the clinopyroxenes are augites in the Kapili and Maharajgunj komatiitic rocks (**Appendix 02: Fig. S1a**). Serpentine shows a wide range of $SiO_2$ and MgO contents coupled with low $Al_2O_3$. Amphiboles from the northern Maharajgunj and southern Kapili sections are mainly tremolite whereas low modal abundances of magnesio-hornblende and actinolite are also found in the southern Kapili section (**Appendix 2: Fig. S1**). Chlorites are Mg-rich with variable $Al_2O_3$, and are identified as corundophilite and sheridanite (**Appendix 2: Fig. S1**). Chlorite grains surrounding the type-II and type-III chromite grains in the Kapili area have higher $Cr_2O_3$ (0.74 - 0.98 wt.%) than chlorite grains from other petrographic contexts ($Cr_2O_3$ = 0.21 - 0.69 wt.%). The carbonate minerals are mainly dolomite in the Tua Dungri komatiitic rocks and calcite in Chuka Pahar (**Appendix 2: Fig. S1**).

### Oxide mineral chemistry

Representative compositional ranges for chromites are tabulated in **Table 2**; all individual analyses are presented in **Appendix 3: Table S2**. The cores of the type-I grains from Tua Dungri have relatively higher MgO, $Cr_2O_3$, $Al_2O_3$, and lower $Fe_2O_3$ (higher Mg# and lower Cr#) than in the outer ferritchromit and chrome magnetite rims (**Fig. 5a**). The non-porous cores of the type-II chromites from the southern Kapili also have relatively higher $Cr_2O_3$ (higher Mg# and lower Cr#) than the porous ferritchromit and chrome magnetite rims (**Fig. 5b**). In both cases, the higher Cr# in the rims reflect the extremely low $Al_2O_3$ contents of these zones rather than a high abundance of $Cr_2O_3$. The central zones of the type-III chromite grains from the northern Kapili have similar concentrations of $Al_2O_3$, $Cr_2O_3$, MgO, and $Fe_2O_3$ (with a wide range of Mg# and Cr#) to those of the type-II grain cores, and are surrounded by rims of various reflectance and porosity (**Fig. 5c**). These pores in the type-II and type-III grains are filled with chrome-chlorite ($Cr_2O_3$ ~1 wt.%). The inner rims of variable reflectance of the type-III grains that have metamorphosed under the amphibolite facies show lower $Fe_2O_3$ and higher $Al_2O_3$ than the inner rims of the type-I and type-II grains (**Fig. 5c**). Outer chrome magnetite rims show compositional similarity in the three types of zoned chromite grains (**Figs. 5**). The type-IV oxides are compositionally similar to ferritchromit rims of the type-I grains, whereas the type-V chrome magnetite grains have similar FeO, $Fe_2O_3$ to those of the chrome magnetite rims (**Table 2**). The cores of both type-I and type-II chromites have higher MnO and ZnO than the rims (**Fig. 5a, b**). The inner rims of the type-II chromites from the northern Kapili have higher $TiO_2$ than the core (**Fig. 5a, b**), whereas the inner rims of the type-III chromites from the southern Kapili have relatively higher $TiO_2$, $V_2O_5$, ZnO, and MnO than the outer porous chrome magnetite rims or the central cores (**Fig. 5b, c; Table 2**). The homogenous type-IV grains have similar $TiO_2$ concentrations, but higher MnO and ZnO than, the ferritchromit rims of the type-I and type-II grains (**Table 2**). Type-V chrome magnetite grains have low concentrations of ZnO (<1 wt.%) with variable $TiO_2$ and MnO (**Table 2**).

The compositions of the type-I cores are clustered in two different places in the Mg# vs. Cr# plots where the smaller grains show higher Al depletion than the coarser grains (**Fig. 6a**). This dichotomy is also evident in the Mg# vs. $Fe^{3+}/R^{+3}$ plot, where the smaller type-1 cores show much greater $Fe^{3+}$ enrichment than the larger ones (**Fig. 6c**). In the same figure, the composition of chrome magnetite rims for all types of chromites and the independent type-V oxide grains occupy the metamorphogenic chrome magnetite field of Barnes and Roeder (2001; **Fig. 6c**). The altered rims for all chromites and the type-V grains define two negative trends in the $TiO_2$ vs. $Fe^{3+}/R^{+3}$ plot (**Fig. 6d**). Almost all chromite rims, as well as type-IV and V grains, also show two distinct negative correlations in the MnO vs. $Fe^{3+}/R^{3+}$ plot (**Fig. 6e**).

In contrast, the zoned chromites show a broad positive trend in the NiO vs. $Fe^{3+}/R^{+3}$ plot (**Fig. 6f**). In a Cr-Al-$Fe^{3+}$ ternary plot, the cores of the smaller type-I grains from Tua Dungri and the type-IV, type-V grains, and most of the ferritchromit to chrome magnetite rims show a variation along the Cr-$Fe^{3+}$ join (**Fig. 6g**), and occupy the field of metamorphogenic ferritchromit-magnetites of Barnes and Roeder (2001). In this ternary diagram the Al-rich type-I cores plot closer to the Cr-Al join, while the cores of the type-II and type-III chromites of the Kapili plot closer to the Cr apex (**Fig. 6g**).

**LA-ICPMS of chromite, ferritchromit, and chrome magnetite: trace elements**

*In situ* trace element analysis by LA-ICPMS of type-I, type-II and type-V oxides show significant compositional variations across the grains (**Fig. 7; Table 3; Appendix 3: Table S3**). Type-III and type-IV grains were not analysed because they are either highly porous (type-III) or small and fractured (type-IV) (**Fig. 3g, 5c**). The type-I zoned chromite grains are from the northern part, whereas the type-II grains are from the southern part of the greenstone belt. The trace element distribution in these zoned chromites demonstrates the change from lower to higher metamorphic grade towards the south. Except for Zn, the concentrations of the minor elements (Sc, Ni, Co, Mn, Ga, and Ti ) are higher in the type-II chromite cores than in the type-I chromite cores (**Fig. 7; Table S3**). The cores of the type-I chromites in the Tua Dungri komatiitic peridotite (northern sector) have higher concentrations of Sc, V, Zn, and Ga than their corresponding rims whereas Ti, Mn, and Ni are higher in most ferritchromit and chrome magnetite rims than in the cores **(Fig. 7a, b; Table 3).** The type-II chromite cores in the Kapili peridotite (southern sector) have higher concentrations of Sc, Ti, V, Mn, Co, Ni, Zn, and Ga than the chrome magnetite rim (**Fig. 7c, d; Table 3**). The type-V chrome magnetite grains show highly variable concentrations of Ti, V, Mn, Co, Ni, Zn, Ga, and Sc (**Table 3**). In Mg# vs. trace elements plots, Ga, Sc concentrations of the type-I chromites cores show a positive correlation from outer to inner core, whereas Ni, Co, Mn, Zn, and Ti show a negative trend (**Fig. 8**). Nevertheless, given the limited number of measurements generalizations must be viewed with caution.

In the trace element spidergram (**Fig. 9a**) the average core compositions of the type-I (n = 4) and type-II (n=2) chromites show a minor negative Sc anomaly (0.79 - 0.86 × EPR MORB Cr-spinel) with high abundances of Zn, Co, and Mn (6.70 - 41.47 × EPR MORB Cr-spinel). The ferritchromit and chrome magnetite rims of the type-I grains (n = 6) also show moderately high abundances of Zn and Mn (5.90 - 8.69 × EPR MORB Cr-spinel) with a strong negative Sc anomaly (0.07 - 0.08 × EPR MORB Cr-spinel). The M-shaped positive anomaly in the segment Zn-Co-Mn (ZCM anomaly; Colás et al. 2014) is more prominent for the rims relative to the cores of the type-I grains (**Fig. 9a**). Chrome magnetite rims of the type-II grains (n = 2) and the average type-V grains (n = 15) have similar patterns, with negative anomalies of Sc (0.09 - 0.10 × EPR MORB Cr-spinel) and minor ZCM anomalies (1 - 5.79 × EPR MORB Cr-spinel) (**Fig. 9a**). The least altered volcanic chromites from other occurrences do not have any such ZCM anomalies and overall show a flat pattern (**Fig. 9b**).

### LA-ICPMS of chromite and chrome magnetite: PGE

Platinum-group elements were determined *in situ* by LA-ICPMS in the cores and rims of type-I and type-II zoned chromites, and type-V chrome magnetite grains (**Fig. 7**; **Table 3; Appendix 3: Table S4**). Type-III and type-IV chromites were avoided for the reasons explained above. Os, Ir, Ru (IPGE), and Rh concentrations were determined successfully, whereas Pt and Pd were below the detection limits in all analysed grains. Despite the mostly uniform count rates of IPGE + Rh, a few grains of the type-V chrome magnetite from the Chuka Pahar (2 points) and Maharajgunj sections (3 points) show anomalous Ru, Rh signals in the time-resolved LA-ICPMS spectra (**Fig. 10; Appendix 3: Table S4**), likely indicating the presence of PGE rich micro-inclusions. The concentrations for these three points from Maharajgunj are determined by averaging the data after excluding the Ru and Rh spikes. However, the PGE spikes were more difficult to unambiguously identify in the two points from Chuka Pahar, and so these spikes are not excluded from the average values (Ru = 128 and 140 ppb, Rh = 4.8 and 8.9 ppb, Os = 22.5 and 25.6 ppb, Ir = 20.8 and 23.8 ppb) given for these two points (LA points 11 and 12) in **Table S4**. For this reason, these two points are not used in the plots in figures 11 and 12. The type-V chrome magnetites in the komatiitic sequence from the Maharajgunj-Chuka Pahar and Kapili sections have different PGE abundances (**Table 4; Table S4**). The type-V grains from Kapili have Os, Ir, Rh below the detection limit with Ru = 8 - 46 ppb except for one data point with Ru = 211 ppb, Rh = 14 ppb, Os = 7ppb, and Ir = 14 ppb compared to the type-V grains from the Maharajgunj-Chuka Pahar section which have higher Os, Ir, Ru and Rh contents (**Appendix 2: Fig. S3**).

The cores of the analysed type-I chromites have lower Ru contents than those of their respective ferritchromit and chrome magnetite rims (**Fig. 7a, b**). Rh content is also slightly lower in the cores of the type-I grains than the rims (**Fig. 7a, b**). Osmium is detected in one laser point of a type-I chromite core (Os = 8.8 ppb). In comparison with the type-I grains, the type-II chromite cores have lower concentrations of Ru and Rh, and similar Ir and Os (**Fig. 7c, d**). The chrome magnetite rims of the type-II grains have a lower concentration of Ru than their respective cores with Rh, Os, and Ir below the detection limit (**Fig. 7c, d**). Overall, the cores of the type-I and type-II zoned chromites from the Gorumahishani belt have lower IPGE + Rh contents than the volcanic chromites of komatiites from Finland, Alexo mine, Pyke Hill, and picrites from Greenland, Kamchatka, Troodos, and the Emeishan province, which have ranges of Ru = 87 - 336 ppb, Rh = 7 - 95 ppb, Ir = 14 - 101 ppb, and Os = 5 - 64 ppb (Puchtel et al. 2004; Park et al. 2017) (**Fig. 11b**).

Primitive mantle normalized plots of Ru, Rh, Os, and Ir show fractionated PGE patterns for all three types of chromites with all being strongly enriched in Ru. In nearly all cases, $Ir_N/Os_N$ ratios are close to 1 (**Fig. 11a; Table 4**). Type-I chromite cores, ferritchromit, and chrome magnetite rims are particularly enriched in both Ru and Rh (15 - 34 × PM). The cores and ferritchromit rims of the type-I chromites tend to have less fractionated PGE ratios than the type-I chrome-magnetite rims (**Table 4**), though given the small number of points it is difficult to generalize. The type-II chromite cores show strong positive anomalies for Ru (16 - 21 × PM) with lower Rh abundances than the type-I grains (**Fig. 11a**). The type-V chrome magnetites are enriched in Os and Ir (Os = 2 - 8 × PM) compared to the other types of chromites) (**Fig. 11a**). They also have low Rh abundances, similar to those of the type-II chromite cores. The least altered volcanic chromites from Troodos, Greenland, Finland, Emeishan picrite and Finland komatiite (Park et al. 2017) show similar PGE patterns of the type-V chrome magnetite grains except Kamchatka picrite (**Fig. 11b**). They have higher Ru anomaly (15 - 56 × PM) but similar abundance of Os, Ir, and Rh. No distinct relationships are observed in V, Ni vs. Ru plots for the type-I, type-II, and type-V grains (**Fig. 12**).

## Discussion

### Modification of chromite to ferritchromit and chrome magnetite during metamorphism

Zones of various reflectances around chromite cores of all types mainly reflect compositional variation in the rims between ferritchromit and chrome magnetite resulting from prograde (Evans and Frost 1975; Burkhard 1993; Loferski 1986; Fleet, 1993; Barnes 2000; Mondal et al. 2006; Mukherjee et al. 2010, 2015) or retrograde metamorphism (Proenza et al. 2004; Gervilla et al. 2012, 2019; Colás et al. 2014, 2017, 2019, 2020). The ferritchromit formation is contemporaneous with modification of the primary mineral assemblages of komatiitic peridotites (olivine, orthopyroxene, clinopyroxene) from cumulate and spinifex zones to serpentine, tremolite, and chlorite. The $H_2O$ and $CO_2$-rich fluid at low metamorphic grade drives the formation of talc, tremolite, chlorite, and carbonate minerals (e.g. Barnes 2006). The komatiitic chromites from the Gorumahishani belt were also modified during metamorphism of the entire greenstone sequence and became depleted in Mg, Al, Cr, and enriched in $Fe^{3+}$ at the boundaries (**Figs. 5, 7**). Chrome-chlorite was formed during this metamorphic process, incorporating Cr and Al released from chromites (e.g. Evans and Frost 1975; Burkhard 1993; Barnes 2000). The enrichment of $Fe^{3+}$ by the oxidation of $Fe^{2+}$ during prograde metamorphism have produced the ferritchromit as the inner rim and chrome magnetite as the outer rim in the modified chromites (type-I and type-II grains; **Fig. 7**). The porous chrome magnetite rims of the type-II grains suggest significant mass loss due to elemental exchange with silicates without any changes in grain size during metamorphism associated with interaction with $CO_2$ and $H_2O$ - rich fluids (**Fig. 5b**). The type-III chromites from the northern Kapili are different from type-I and type-II grains, showing complex zoning patterns with a highly porous character (**Fig. 5c**). These grains have broadly higher Cr# (0.87 - 0.92) and lower Mg# (0.08 - 0.17) in their cores relative to type-I varieties (**Fig. 5c**). Lower $Fe_2O_3$ (2.1-14.88 wt.%) and $Fe^{3+}/R^{3+}$ in the type-I and II inner rims relative to the outer rims suggest the slow progression of the oxidizing fluids. The co-existing mineral assemblages associated with type-III and type-II grains are similar except for the lower modal abundance of chlorite in the former. The higher $Al_2O_3$ in the inner rims of the type-III grains might be due to the breakdown of chlorite under amphibolite facies metamorphism (e.g. Loferski 1986). The type-IV grains from Maharajgunj are intensely fractured small ferritchromit grains suggesting deformation during metamorphism (**Fig. 3g**). The concentrations of major and minor elements in the type-IV grains are mostly similar to those in the ferritchromit rims of the type-I and type-II grains. The mineral assemblage of serpentine + chlorite + carbonate + talc ± tremolite from the northern Tua Dungri indicates a low metamorphic grade close to the greenschist-amphibolite transition (**Fig. 4**). The type-V chrome magnetite to magnetite grains have wide-ranging major and minor element concentrations (**Fig. 6; Table S3**) and the geochemical diversity reflects the differing degrees of metamorphism related to the development of the chrome magnetite grains. Finer-grained type-V magnetite grains were formed during modification of the primary ferromagnesian silicates during hydration of the komatiitic rocks (e.g. Bach et al. 2004; Alt et al. 2007; Gahlan et al. 2006; Eslami et al. 2018).

Considering the olivine core ($Fo_{88}$) from the Kapili area (**Fig. 3a**) and the associated chromite core, the geothermometers of Roeder et al. (1979) and Fabriès (1979) reveal re-equilibration temperatures in the range of 409°-619°C, consistent with amphibolite facies metamorphism. However this olivine grain is potentially of metamorphic origin because in the amphibolite facies serpentine breaks down to form metamorphic olivine (e.g. Barnes 2006). Thermometric calculations are also performed using chrome magnetite-ilmenite pairs of the Maharajgunj (1 pair) and Kapili area (3 pairs) following the method of Spencer and Lindsley (1981) and Lepage (2003). The calculated temperature from the northern part of the greenstone belt (Maharajgunj area) is 384°C suggesting greenschist facies metamorphism at $X(CO_2) < 0.05$ in the stability field of serpentine, tremolite, chlorite, and carbonate (e.g. Barnes 2006). On the other hand, the calculated temperatures from the southern part of the greenstone belt (Kapili area) range from 443 to 502 °C suggesting amphibolite facies metamorphism at $X(CO_2) < 0.05$ in the stability field of serpentine, tremolite, chlorite, ± metamorphic olivine, which is consistent with our observations (e.g. Barnes 2006).

### ***In situ* LA-ICPMS study of the komatiitic chromites: Fractionation of trace elements**

Zoned chromites from the Gorumahishani belt show inter- and intra-grain major and minor element variations, developed due to greenschist to amphibolite facies metamorphism. Similar variations are apparent in trace element abundances determined by LA-ICPMS. The positive relationships of Ga, Sc with Mg# for the non-porous cores of type-I chromites indicate relatively pristine core compositions (**Fig. 8a, b**). However, the sum of Zn + Co + Mn remains almost constant with decreasing Ga (**Fig. 8h**). This indicates a greater role for metamorphism than for $H_2O$, $CO_2$ - rich fluid activity because hydrothermal re-equilibration might have affected the Zn + Co + Mn content of type-I cores (e.g. Colás et al. 2014) but not Ga. Ga and Sc are not compatible in olivine but may enter into the chlorite structure in substitution for Al during metamorphic modification of the assemblage. Relatively abundant chlorite in the Tua Dungri komatiitic peridotites thus justifies the lower contents of Ga and Sc in the $Fe^{3+}$-rich rims than in the cores of the type-I chromites (**Fig. 7a, b**).

The type-II porous chromites have a higher concentration of Ga and similar Sc compared to the type-I grains (**Appendix 2: Fig. S2a; Table 3**). The higher concentrations of Ga and lower modes of chlorite in the pores of chrome magnetite rims from Kapili suggest a lower degree of substitution of Ga for Al in chlorite. Lower $Al_2O_3$ contents in the type-II cores and rims than in the type-I variety support this observation as Al has migrated to chlorite (**Table 3**). The concentrations of Zn in the type-II cores are similar but Co and Mn are higher compared to the type-I cores (**Table 3; Fig. 9**). This is related to the higher metamorphic grade i.e. amphibolite facies metamorphism suffered by the komatiitic rocks of Kapili and therefore, higher diffusion rate of the trace elements (e.g. Sievwright et al. 2020). The ZCM anomaly in the type-I and type-II chromite cores (**Fig. 9**) was likely due to modification during metamorphism when Zn, Co, and Mn were diffused into the chromite structure from altered silicate minerals such as olivine, clinopyroxene, and the associated carbonate phases (e.g. Colás et al. 2014).

The microprobe data are consistent with the LA-ICPMS data and show greater contrast between core and rim in the type-III grains than in the type-II grains, with the inner rims of the former having higher concentrations of Mn, Zn, Ni, Ti, and V than the cores (**Table 2**). This transition from homogenized type-II cores towards enriched type-III inner rims indicates the reverse diffusion of these elements from the core to the inner rims of the type-III grains after complete homogenization of core composition under the amphibolite facies conditions (e.g. Barnes 2000) (**Fig. 13**).

The LA-ICPMS data show that the type-II cores have higher concentrations of Ni (4513 - 10583 ppm) and Ti (20759 - 36413 ppm) at similar Mg# (0.13 - 0.16) and higher $Fe^{3+}/R^{3+}$ ratio (0.08 - 0.10) than the type-I cores (**Fig. 8**; **Table 3)**. $Ti^{4+}$ is less mobile to incorporate into the spinel structure than the +2 ions (e.g. Barnes 2000), therefore, its higher concentration in type-II cores indicates a homogenized character than the type-I cores under a higher grade of metamorphism (**Fig. 13**). With increasing $Fe^{3+}/R^{3+}$ ratio, bivalent ions begin to occupy octahedral sites of the inverse spinel structure (e.g. Barnes 2000; Gervilla et al. 2012). As the homogenized type-II cores have higher $Fe^{3+}/R^{3+}$ ratios, their higher Ni concentrations may therefore result from the substitution of $Ni^{2+}$ for the bivalent ions ($Fe^{2+}$, $Mg^{2+}$) in the divalent octahedral sites and $Ti^{4+}$ for $Fe^{3+}$ in the tetrahedral sites (e.g. Barnes 1998, 2000).

The type-V chrome magnetite grains show variable degrees of enrichment of Zn and Co with lower Mg# and higher $Fe^{3+}/R^{3+}$ ratios (**Fig. 8d, f; Table 3**), indicating different degrees of involvement of metamorphism. However, the overall negative relationship between $Fe^{3+}/R^{3+}$ and Mn mainly from the type-V grains (**Fig. 6e**) indicates the bivalent tetrahedral site occupancy of Mn was decreased in the inverse spinel structure. $Fe^{3+}$occupies the tetrahedral site in the inverse spinel structure, limiting the possibility of Mn occupying this site (e.g. Sack and Ghiorso 1991; González Jiménez et al. 2009; Gervilla et al. 2012). The type-V chrome magnetite grains also show variable enrichment of Ni and Ti with Mg# and $Fe^{3+}/R^{3+}$ (**Fig. 8b, g; Table 3**). This is due to different degrees of metamorphic modification coupled with a variable $Fe^{2+}$-$Fe^{3+}$ re-ordering (e.g. Barnes 2000; Gervilla et al. 2012).

### ***In situ* LA-ICPMS study of the Gorumahishani komatiitic chromites: Fractionation of PGE**

Previous studies using *in situ* LA-ICPMS analysis of natural Cr-spinels from volcanic ultramafic-mafic rocks have documented higher concentrations of Rh, Os, Ir, and Ru that are considered to be present as solid solutions in the spinel structure (Locmelis et al. 2011; Park et al. 2012, 2017; Pagé et al. 2012; Pagé and Barnes 2016). Platinum-group elements were also found to exist as micro-nuggets in chromite grains (Tredoux et al. 1995; Ballhaus and Sylvester 2000; Park et al. 2012, 2017; Kamentsky et al. 2015; Arguin et al. 2016). Inclusions of PGE-bearing phases, such as laurite ($RuS_2$), IPGE-alloys, and Pt-alloys are common in chromites from mafic layered intrusions and ophiolitic complexes (Garuri et al. 2002; Ahmed 2007; Fonseca et al. 2009; Habtoor et al. 2017; Prichard et al. 2017; Mondal et al. 2019b and references therein). Experimental studies considering silicate melt and chrome-spinel have shown higher partition coefficients of Rh and IPGEs (Os, Ir, Ru) in chrome-spinels than Pt, Pd (Capobianco and Drake 1990; Nell and O'Neill 1997; Righter and Downs 2001; Brenan et al. 2012).

*In situ* LA-ICPMS analysis of type-I, type-II, and type-V grains show high Ir, Os, Ru, and Rh concentrations with strong positive Ru anomalies (**Fig. 11a**), as observed in other volcanic chromites in a variety of contexts (**Fig. 11b**) (e.g. Park et al. 2017). However, the concentrations of Rh, Ir, Os, and Ru differ between the types of altered chromite grains and are also highly variable in different zones within a single grain (**Fig. 7; Table 4**). The type-I chromite cores from Tua Dungri have lower Ru and similar Ir and Os to the ferritchromit and chrome magnetite rims (**Fig. 7a, b)**. The Rh concentrations are also slightly lower in the cores of the type-I grains than in the corresponding outer ferritchromit and chrome magnetite rims (**Fig. 7a, b; Table 4**). The petrological evidence reveals that the type-I chromite grains were modified under greenschist-amphibolite transition facies conditions. The modification of existing chromite to ferritchromit and chrome magnetite rims was accompanied by the development of an inverse spinel structure surrounding the core. Among the PGEs, $Rh^{2+}$ might have diffused towards the ferritchromit and chrome magnetite rims as these elements prefer to occupy divalent octahedral sites of inverse spinel (e.g. Borisov and Palme 1995; Brenan et al., 2003; Park et al. 2017). However, such a process, if it occurred, must have been quite limited as the difference between the Rh abundances of the core and the rim are minimal (**Fig. 7a, b**).

Ru shows no relationship with Ni or V contents despite the fact that these trace elements also tend to occupy the divalent octahedral sites in an inverse spinel structure (**Fig. 12a, b**) (e.g. Barnes 2000; Park et al. 2017). Ruthenium exists both as $Ru^{2+}$ and $Ru^{3+}$ depending on the $fO_2$ condition of the magma (e.g. Brenan et al., 2012; Park et al. 2012; Locmelis et al. 2018). If Ru occupied the divalent octahedral site as $Ru^{2+}$, the type-I chromite grains should have crystallized from a reduced parental melt. However, the $Fe^{3+}$ enrichment and development of an inverse spinel structure during formation of the ferritchromit and chrome magnetite rims were due to post magmatic oxidation during metamorphism and not a magmatic process. Therefore, it is possible that Ru was initially present as a $2^{+}$ ion in the reduced komatiitic melt of the early Archean Gorumahishani greenstone belt and thus preferred to occupy the divalent octahedral sites ($Ru^{2+}$) in the primary magmatic chromites.

The enrichment of $Ru^{2+}$ in the outer rims took place during metamorphic modification of the grains when $Ru^{2+}$ preferentially diffused to the octahedral sites in the inverse spinel structure of the rims (**Fig. 7a, b**). Vanadium (V) is a redox sensitive element, and during metamorphic modification of chromites the concentrations should be increased in the altered outer rims, however, there is no such correlation of V with Ru concentrations in the zoned chromites (**Fig. 12**). This suggests a reduced mantle source for the Gorumahisani komatiites and consistent with the earlier observation of a global heterogeneity in mantle redox conditions as inferred from the early Archean komatiitic melts (e.g. Nicklas et al. (2019).

As noted above, there may also be some IPGE-bearing phases present as inclusions (e.g. laurite, erlichmanite, IPGE alloys; Kamentsky et al. 2015) which result in the IPGE-enrichment of chrome-spinels (e.g. chrome-spinels from komatiitic, ferropicritic, and tholeiitic basalt from the Abitibi Greenstone belt; Fiorentini et al. 2004). A minor IPGE spike (Rh, Ru rich inclusion) is observed from the LA spots in the type-I grains (**Fig. 10**), however, only a limited number of spots were analysed and no specific platinum-group mineral phase was identified during the SEM study. In addition, the observation of Ru (and Rh) enrichments in the outer rims on both sides of the central cores of the type-I grains strongly suggests that in the studied spots Ru is hosted as a solid solution in the spinel structure rather than in IPGE bearing inclusions (**Fig. 7a, b**).

The type-II chromite cores have lower Os, Ir, Ru, and Rh than the type-I chromite cores (**Fig. 7c, d; Table 4**). In addition, the chrome magnetite rims of the type-II grains have a negligible amount of Ru with no traceable Rh, Os, and Ir (**Fig. 7c, d; Table 4**). The petrological evidence reveals that the type-II chromite grains were modified under amphibolite facies conditions. Therefore, enrichment of Ru and Rh in the thick chrome magnetite rims relative to the cores should have been even higher than in the type-I grains. The very low abundances of these elements in both type-II cores and rims are thus surprising, and may reflect faster diffusion under the higher metamorphic grade (**Fig. 13**). The chalcophile character of PGEs might have facilitated the partitioning of these elements into the co-existing sulfide phases (e.g. chalcopyrite, pentlandite, millerite) or platinum-group minerals (e.g. laurite, erlichmanite, IPGE alloy) that may be present in the komatiitic rocks or as inclusions in Kapili chromites (Peach and Mathez 1996; Andrews and Brenan 2002; Fiorentini et al. 2004; Fonseca et al. 2009; Pagé and Barnes 2016; Park et al. 2012, 2017; Locmelis et al. 2018).

The isolated type-V chrome magnetite grains have higher Os, Ir, and lower Rh content with a wider range of Ru concentration than the cores and rims of type-I and type-II grains (**Table 4**). The IPGE and Rh concentrations of type-V grains vary spatially in the greenstone belt (**Appendix 2: Fig. S3**). Only Ru is detected in type-V grains from the southern Kapili area whereas higher IPGE and Rh contents are found in those from the northernmost Maharajgunj and Chuka Pahar areas (**Table 4**). The overall enrichment of Os and Ir in the type-V grains (**Fig. 11; Table 4**) is due to the stronger affinity of these elements towards the VI-fold coordination of the inverse spinel structure (e.g. Brenan et al. 2012).

### Mass balance calculations and determination of empirical partition coefficients of trace elements and PGE between chromite and komatiitic melt

Chrome-spinel plays a significant role in controlling the budget of IPGE and Rh, and several trace elements in plutonic and volcanic ultramafic-mafic rocks. Thus understanding the partitioning of these elements between ultramafic-mafic silicate melt and co-existing chrome-spinels during early magmatic processes is of great importance. This is a challenging exercise for the Gorumahishani komatiitic chromites owing to their extensive alteration and therefore, only the core compositions of the least altered chromites were considered for these calculations. We have considered the compositions of the Al-depleted meta-peridotite from Tua Dungri (sample MIC/16/44) and the Al-enriched meta-peridotite from Kapili (sample SHB/18/25) (values in **Appendix 3: Table S5**) to be equivalent to the parental komatiitic melt compositions of the type-I (Tua Dungri) and type-II (Kapili) chromites, respectively.

We first calculated the mass fraction of chromite in komatiitic rocks from the least altered chromite cores of type-I (sample MIC/16/39, meta-peridotite) and type-II grains (sample SHB/19-12/82, spinifex-textured meta-peridotite) following the equation proposed by Pagé and Barnes (2016):

$$\text{\% Cr-spinel in sample} = (Cr_2O_3^{WR} / Cr_2O_3^{Cr\text{-}spinel})*100*0.75$$

where $Cr_2O_3^{WR}$ = whole-rock $Cr_2O_3$ content in wt.% and $Cr_2O_3^{Cr\text{-}spinel}$ = $Cr_2O_3$ content of Cr-spinel in wt.%. The calculation assumes that 75% of Cr in the whole rock is hosted by chromite (e.g. Arguin et al. 2016), with the rest being hosted by silicate phases dominated by olivine with some pyroxene (e.g. Pagé et al. 2012; Pagé and Barnes 2016). Using the $Cr_2O_3$ abundances of the least altered chromite cores and the $Cr_2O_3$ contents of the corresponding rocks we find that the proportions of chromite in the komatiitic rocks ranged from 0.33% to 0.61% (**Appendix 3: Table S6, S7**) which is similar to the lower limit of chromite modal abundances obtained by Pagé and Barnes (2016) for volcanic samples. The weight fraction of chromite in the studied samples was used to estimate the fractions of trace elements and IPGE + Rh in the whole rock contributed by chromite, following the equation of Pagé and Barnes (2016):

$$F_i^{Cr\text{-}spinel} (\%) = 100* (C_i^{Cr\text{-}spinel} * F^{Cr\text{-}spinel}) / C_i^{WR}$$

where $F_i^{Cr\text{-}spinel}$ = contribution of element ‘i’ from chromite in the whole rock, $C_i^{Cr\text{-}spinel}$ =

element ‘i’ concentration in chromite, $F^{Cr\text{-}spinel}$ = proportion of Cr-spinel in our sample, and $C_i^{WR}$ = concentration of element ‘i’ in the whole-rock. The mass balance calculation for the Tua Dungri komatiites indicates that chromite hosts mass fractions of Sc = 0.12 - 0.15%, Ti = 0.04%, Ni = 0.08 - 0.10%, V = 4.46%, Ga = 2.71 - 3.62%, Mn = 0.83 - 0.87% and Co = 3.7 - 3.92%. The proportions for the Kapili komatiites are: Sc = 0.09 - 0.16%, Ti = 3.89 - 7.05%, Ni = 2.88 - 6.97%, Ga = 6.58 - 11.41%, Mn = 9.62 - 16.78%, Co = 12.33 - 18.87% and V = 18.20 - 40.34% (**Appendix 3: Table S6, S7**). These values can be compared with the $F_{Sc}$, $F_{Ni}$, and $F_V$ values of the least modified komatiitic chromites ($F_{Sc}$ = 23.21%, $F_{Ni}$ = 47.98%) of Park et al. (2017) and the bulk rock data of Törmänen et al. (2016). Assuming that our choices for the bulk melt compositions are appropriate, the data show that low and variable fractions of the considered minor and trace elements are hosted by chromites in the the Gorumahishani komatiites, unlike the much higher fractions of these elements hosted by chromites in the other komatiites (e.g., Park et al 2017). This suggests that the distribution of these elements in the komatiitic rocks is mainly controlled by the modally abundant silicate or carbonate minerals in combination with the metamorphic modification of the primary assemblages.

Calculations based on global komatiitic and ultramafic-mafic volcanic rocks (e.g. Pagé et al. 2012; Pagé and Barnes 2016; Park et al. 2017) reveal that about 15 - 40% of the whole-rock Os, Ir, Rh budgets and nearly 100% of the Ru budget are represented by accessory chromites or the PGE-rich micro-inclusions they contain. In contrast, the type-I chromite cores from the Gorumahishani komatiites account for 15-20% Ru, 11-12% Rh, 2% Os and 1-2% Ir in the whole-rock budgets while the type-II chromite cores represent even lower proportions of these elements (Ru ~8-10%, Rh ~2%, Os ~2%, and Ir ~1%; **Appendix 3: Table S6, S7**) (**Fig. 11b**). The lower values from both types of grains relative to those calculated from the global dataset partly reflect redistribution of PGEs during metamorphic modification of the komatiitic chromites or Cr-spinel crystallization after sulfide saturation of the komatiitic magma. In addition, part of the whole-rock PGE budget may be held by micro-inclusions of PGE-alloys or PGE-minerals in the zoned chrome-spinels, although such phases have not yet been identified in the laser spot analyses of our samples (Fiorentini et al. 2004; Barnes and Fiorentini 2008; Park et al. 2012; Arguin et al. 2016). Metamorphic redistribution may include diffusion of IPGE and Rh from chromites to co-existing sulfide phases (e.g. chalcopyrite, pentlandite, millerite). Low chromite abundance in the Gorumahishani komatiites can also be responsible for their low contribution to the whole-rock IPGE + Rh budget as their proportion is similar to the lower limit of chrome-spinel present in the rocks studied by Page and Barnes (2016).

We have calculated the empirical partition coefficients for trace elements and PGEs considering the chromite core compositions and the bulk rock compositions of the selected komatiitic rocks (Table S5). To obtain the composition of the melt with which the Cr-spinel equilibrated, it is necessary to exclude the portion of each element hosted by this phase from the bulk rock composition. To do this, we used the mass balance equation as formulated by Pagé and Barnes (2016):

$$C_i^{Melt} = [(C_i^{WR}*100)-(C_i^{Cr\text{-}spinel}*\%\ Cr\text{-}spinel)]/\ (100\text{-}\%\ Cr\text{-}spinel)$$

where $C_i^{Melt}$ = content of element 'i' in the silicate melt. We then used these calculated melt compositions to determine empirical partition coefficients ($D = C_i^{Cr\text{-}spinel}/C_i^{Melt}$) for Sc, Ti, V, Mn, Co, Ni, Ga, IPGEs, and Rh for the least altered type-I and type-II cores. Type-I chromite cores have values of $D_{Sc}$ = 0.37 - 0.45, $D_{Ni}$ = 0.24 - 0.28, $D_{Ti}$ = 0.12 - 0.13, and $D_{Co}$ = 11.58 - 12.10 (**Table 5**) similar to or lower than previous empirical values for volcanic chromites as well as experimentally determined values e.g. $D_{Sc}$ = 0.36 - 0.57, $D_{Ni}$ = 3.5 - 6.8 and $D_{Ti}$ = 0.4 - 3.5, $D_{Co}$ = 3.1 - 29.6 (Horn et al. 1994; Sattari et al. 2002; Righter et al. 2006; Pagé and

Barnes 2009; Park et al., 2012). The other trace elements from type-I chromite cores show a restricted range of values: $D_V$ = 14.08 - 14.38, $D_{Mn}$ = 2.51 - 2.69, and $D_{Ga}$ = 8.44 - 11.04 (**Table 5**). The type-II chromites have higher empirical partition coefficients for $D_{Co}$ (23.52 - 37.66) than the type-I values, and even higher than the volcanic chromites determined by previous workers (Horn et al. 1994; Sattari et al. 2002; Righter et al. 2006; Pagé and Barnes 2009; Park et al. 2012). The other trace elements, with the exception of Sc, also show higher values than the type-I values (**Table 5**). Nevertheless, accessory chromites in komatiitic rocks have re-equilibrated with co-existing modally abundant silicate minerals during metamorphism, so the empirically determined partition coefficients should differ from the true magmatic values.

Empirical partition coefficients calculated for IPGEs and Rh for type-I chromite cores are $D_{Os}$ = 4.45, $D_{Ir}$ = 2.54 - 4.18, $D_{Ru}$ = 49.79 - 67.86, and $D_{Rh}$ = 32.21 - 36.94 (**Table 6**). Coefficients for type-II chromite cores are $D_{Ir}$ = 2.23 - 3.1, $D_{Ru}$ = 35.51 - 45.43, and $D_{Rh}$ = 4.4 - 4.94, which are lower than the values obtained for the type-I grains except for $D_{Os}$ = 8.18 - 8.45 (**Table 6**). Previous studies (e.g. Pagé et al. 2012; Park et al. 2017) of komatiitic chromites yielded $D_{Os}$ = 9.6 - 18, $D_{Ir}$ = 11 - 11.8, $D_{Ru}$ = 5.64 - 100, and $D_{Rh}$ = 13 - 18.1. The calculated $D_{Os}$ and $D_{Ir}$ from this study are somewhat lower while $D_{Ru}$ falls within the wide range of published values. $D_{Rh}$ shows lower values in type-II cores but higher in type-I cores compared to the published data. Experiments by Brenan et al. (2012) using synthetic iron-bearing basalt at 0.1 MPa and 2 GPa at 1400 - 1900 °C, $fO_2$ = IW+1.6 to IW+2.1 yielded lower partition coefficient values for these elements ($D_{Ru}$ = 4, $D_{Rh,\ Ir}$ = 0.04 - 1). However, the values were higher ($D_{Ir}$ = 186.9, $D_{Ru}$ = 37.9 and $D_{Rh}$ = 89) under more oxidizing conditions, e.g. $fO_2$ = IW+3.1 to IW+7.2. Other researchers (e.g. Capobianco and Drake 1990; Capobianco et al. 1994; Righter et al. 2004) determined the experimental partition coefficients under much more oxidizing conditions (NNO to HM buffer), obtaining exceedingly high values of $D_{Ir}$ = 5 - 22000, $D_{Ru}$ = 20 - 4000, and $D_{Rh}$ = 41 - 530. Natural chrome-spinels crystallized from an oxidized basaltic magma from Ambae volcano, Vanuatu at $fO_2$ = QFM+2.5 (Park et al. 2012) yielded $D_{Os}$ = 288, $D_{Ir}$ = 472, $D_{Ru}$ = 2448, and $D_{Rh}$ = 641, which are comparable to the values determined experimentally under highly oxidizing conditions. Brenan (2012) emphasized that the high D (Ru Ir, Rh) values obtained for experiments performed under oxidizing conditions were due to the presence of ferric iron in the spinels. In this light, it is significant that some of the zoned chromites from the Gorumahishani belt have $Fe^{3+}$ rich outer rims with elevated Ru and Rh contents. Similarly, many of the type-V chrome magnetites have high IPGE contents (**Table 4**). Although the $fO_2$ values of the Gorumahishani komatiite parental melts are poorly constrained, the empirical partition coefficients ($D_{IPGE, Rh}$) of this study and comparison with other natural or experimental values suggest that the accessory chromites we studied might have crystallized from magma under relatively low $fO_2$ conditions. The low calculated D values for Os, Ir, Ru, and Rh are consistent with the low $Fe^{3+}/R^{3+}$ values of the type-I and type-II chromite cores, with both suggesting reducing conditions. Global heterogeneity in early Archean mantle redox conditions and the change of estimated $fO_2$ conditions for komatiitic melts from reducing to oxidizing since the early Archean (3.48 Ga: 0.11 ± 0.30 ΔQFM log units to 1.87 Ga: +1.22 ± 0.31 ΔQFM log units; Nicklas et al. 2019) supports our observations. Finally, even though the cores are the least altered chromite available, their trace element and PGE abundances may still have been modified by metamorphism. So the calculated magmatic partition coefficients may represent minimum values. This is particularly true for the type-II cores from the southern area (Kapili), which experienced higher grade metamorphism and which are less likely to represent magmatic compositions.

## Conclusions

(1) Komatiitic rocks of the Gorumahishani greenstone belt were metamorphosed under conditions close to the greenschist-amphibolite facies transition in the northern Maharajgunj-Chuka Pahar-Tua Dungri sector and under amphibolite facies conditions in the southern Kapili sector. Accessory komatiitic chromites were modified during metamorphism in the presence of $H_2O$ and $CO_2$-rich fluids by reaction with surrounding primary silicate and oxide minerals. Three types of zoned chromites as well as homogenous grains of ferritchromit and chrome magnetite were developed during this stage by release of Cr, Al, and Mg, and re-ordering of $Fe^{2+}$ - $Fe^{3+}$ in the spinel structure.

(2) As the metamorphic grade increases from the northern to the southern part of the greenstone belt, the type-II chromite cores, found only in the south, display greater extents of diffusive equillibration of trace elements such as Zn, Co, Mn with associated silicate or carbonate minerals than the type-I chromite cores, found only in the north. Increasing IPGE (Os, Ir, Ru) and Rh concentrations from type-I cores to rims and lower concentrations of these elements in type-II chromite cores to undetectable concentrations in type-II rims are also related to the increasing metamorphic grade towards the south. The IPGEs and Rh may also have diffused to the co-existing sulfide minerals such as chalcopyrite, pentlandite, millerite, or platinum-group minerals (e.g. laurite, erlichmanite, IPGE alloy), if present.

(3) Mass balance calculation shows that the cores of the type-I chromite contribute < 1% Sc, Ti, Ni, and Mn, and 2 - 5% V, Ga, and Co to the whole rock trace element budget. The type-II chromite cores contribute <1 - 19% Sc, Ti, Ni, Mn, Ga, Co, and 18 - 40 % V indicating a major control of the modally abundant silicate minerals on the whole rock budget of these trace elements. In terms of IPGE + Rh, the type-I chromite cores contribute ≤ 20% and the type-II

chromite cores contribute ≤ 10% of the whole rock IPGE + Rh budget indicating the effect of metamorphism or equilibration with other PGE-bearing or sulfide phases.

(4) Calculation of empirical partition coefficients (D) of trace and platinum-group elements based on the least altered cores of the type-I and type-II grains and komatiitic whole-rock compositions yield values broadly comparable to natural and experimental values. These values generally fall towards the low end of the experimental range, consistent with partitioning under reducing conditions. The low D values of the type-I and type-II cores may therefore indicate their crystallization from reduced komatiitic melts. These interpretations should be viewed cautiously because of the limited number of *in situ* PGE and trace element data and because the compositions of the chromite cores, particularly those of type-II, may have been modified by metamorphism.

## Acknowledgments

Research for this article has been conducted under the CEFIPRA-Indo-French International Collaborative Project-6007-1 between Sisir Mondal and Laurie Reisberg, and represents a component of the Ph.D. thesis work of CEFIPRA Research Scholar Ratul Banerjee. This study was partly supported by the National Research Foundation of Korea funded by the Ministry of Science and ICT (2022R1A2C1011741) granted to Jung-Woo Park. Two anonymous reviewers of the journal are acknowledged for their useful reviews of this article. Tim Grove, journal Editor-In-Chief is acknowledged for his editorial support and great patience.

## References

Adhikari A, Mukherjee S, Vadlamani R (2021) A plume-mantle interaction model for the petrogenesis of komatiite-komatiitic basalt-basalt-basaltic andesite volcanism from the

Paleoarchean (3.57-3.31 Ga) Iron Ore Group greenstone belts, Singhbhum craton, India: Constraints from trace element geochemistry and Sm-Nd geochronology. Lithos 398-399:106315

Ahmed AH (2007) Diversity of platinum-group minerals in podiform chromitites of the late proterozoic ophiolite, eastern Desert, Egypt: genetic implications. Ore Geol Rev 32:1-19

Alt JC, Shanks WC, Bach W, Paulick H, Garrido CJ, Beaudoin G (2007) Hydrothermal alteration and microbial sulfate reduction in peridotite and gabbro exposed by detachment faulting at the Mid-Atlantic Ridge, 15°20’N (ODP Leg 209): a sulfur and oxygen isotope study. Geochem Geophys Geosyst 8:Q08002

Andrews DRA, Brenan JM (2002) Phase equilibrium constraints on the magmatic origin of laurite + Ru-Os-Ir alloy. Canad Mineral 40:1705-1716

Arguin J-P, Pagé P, Barnes S-J, Yu S-Y, Song X-Y (2016) The Effect of Chromite Crystallization on the Distribution of Osmium, Iridium, Ruthenium and Rhodium in Picritic Magmas: an Example from the Emeishan Large Igneous Province, Southwestern China. J Petrol 57:1019-1048

Arndt NT, Lesher CM, Barnes SJ (2008). Komatiite. Cambridge University Press.

Augé T, Cabri LJ, Legendre O, McMahon G, Cocherie A (1999) PGE distribution in base metal alloys and sulfides of the New Caledonia ophiolite. Can Min 37:1147-1161

Bach W, Garrido CJ, Paulick H, Harvey J, Rosner M (2004) Seawater-peridotite interactions: first insights from ODP Leg 209, MAR 15°N. Geochem. Geophys Geosyst 5(9):Q09F26

Ballhaus C, Sylvester P (2000) Noble metal enrichment processes in the Merensky Reef, Bushveld Complex. J Petrol 41:545-561

Banerjee R, Mondal SK, Reisberg L, Zhou X (2021) Origin of Ni-Cu-sulfide minerals in the komatiitic rock suite of the Archean Gorumahishani Greenstone belt, Singhbhum Craton (eastern India). Virtual Goldschmidt 2021

Barnes SJ, Boyd R, Korneliussen A, Nilsson LP, Often M, Pederson RB, Robins B (1988) The use of mantle normalization and metal ratios in discriminating between the effects of partial melting, crystal fractionation and sulfide segregation on platinum-group elements, gold, nickel and copper: examples from Norway. *In*: Prichard HM, Potts PJ, Bowles JFW, Cribb SJ (eds) Geo-platinum, vol 87. Elsevier, Amsterdam, pp 113–143

Barnes SJ (1998) Chromite in komatiites, 1. Magmatic controls on crystallization and composition. J Petrol 39:1689-1720

Barnes SJ (2000) Chromite in komatiites, II. Modification during greenschist to mid amphibolite facies metamorphism. J Petrol 41:387-409

Barnes SJ, Roeder PL (2001) The Range of Spinel Compositions in Terrestrial Mafic and Ultramafic Rocks. J of Petrol 42:2279-2302

Barnes SJ (2006) Komatiites: Petrology, Volcanology, Metamorphism, and Geochemistry. Econ Geol Spec Publ 13:13-49

Barnes SJ, Fiorentini ML (2008) Iridium, ruthenium and rhodium in komatiite: Evidence for iridium alloy saturation. Chem Geol 257:44-58

Basu AR, Bandyopadhyay PK, Chakrabarti R, Zou H (2008) Late 3.4 Ga Algoma-type BIF in the Eastern Indian Craton. Geochim et Cosmochim Acta 72:A59

Borisov A, Palme H (1995) The solubility of iridium in silicate melts: New data from experiments with $Ir_{10}Pt_{90}$ alloys. Geochim et Cosmochim Acta 59(3):481-485

Brenan JM, McDonough WF, Dalpe C (2003) Experimental constraints on the partitioning of rhenium and some platinum-group elements between olivine and silicate melt. Earth Planet Sci Lett 212:135-150

Brenan JM, Finnigan CF, McDonough WF, Homolova V (2012) Experimental constraints on the partitioning of Ru, Rh, Ir, Pt and Pd between chromite and silicate melt: The importance of ferric iron. Chem Geol 302-303:16-32

Burkhard DJM (1993) Accessory chromian spinels: their coexistence and alteration in serpentinites. Geochim et Cosmochim Acta 57:1297-1306

Cabri LJ, Sylvestor PL, Tubrett MN, Peregoedova A, Laflamme JHG (2003) Comparison of LAM-ICP-MS and micro-PIXE results for palladium and rhodium in selected samples of Noril'sk and Talnakh sulfides. Can Min 41:321-329

Canil D (2002) Vanadium in peridotites, mantle redox and tectonic environments: Archean to present. Earth Planet Sci Lett 195:75-90

Capobianco CJ, Drake MJ (1990) Partitioning of ruthenium, rhodium, and palladium between spinel and silicate melt and implications for platinum group element fractionation trends. Geochim et Cosmochim Acta 54:869-874

Capobianco CJ, Hervig RL, Drake MJ (1994) Experiments on crystal/liquid partitioning of Ru, Rh and Pd for magnetite and hematite solid solutions crystallized from silicate melt. Chem Geol 113:23-43

Chaudhuri T, Mazumder R, Arima M (2015) Petrography and geochemistry of Mesoarchaean komatiites from the eastern Iron Ore belt, Singhbhum craton, India, and its similarity with ‘Barberton type komatiite’. J Afr Earth Sci 101:135-147

Chaudhuri T, Satish-Kumar M, Mazumder R, Biswas S (2017) Geochemistry and Sm- Nd isotopic characteristics of the Paleoarchean Komatiites from Singhbhum Craton, Eastern India and their implications. Precambrian Res 298:385-402

Colás V, González-Jiménez JM, Griffin WL, Fanlo I, Gervilla F, O’Reilly SY, Pearson NJ, Kerestedjian T, Proenza JA (2014) Fingerprints of metamorphism in chromite: new insights from minor and trace elements. Chem Geol 389:137-152

Colás V, Padrón-Navarta JA, González-Jiménez JM, Fanlo I, López Sánchez-Vizcaíno V, Gervilla F, Bolibar R (2017) The role of silica in the hydrous metamorphism of chromite. Ore Geol Rev 90:274-286

Colás V, González-Jiménez JM, Camprubí A, Proenza JA, Griffin WL, Fanlo I, O'Reilly SY, Gervilla F, González-Partida E (2019) A reappraisal of the metamorphic history of the Tehuitzingo chromitite, Puebla state, Mexico. Int Geol Rev 61(7):1706-1727

Colás V, Subias I, González-Jiménez JM, Proenza J, Fanlo I, Camprubí A, Griffin W, Gervilla F, O'Reilly S, Escayola M (2020) Metamorphic fingerprints of Fe-rich chromitites at Eastern Pampean Ranges. Boletin de la Sociedad Geologica Mexicana 72(3):A080420

Droop GTR (1987) A general equation for estimating $Fe^{3+}$ concentrations in ferromagnesian silicates and oxides from microprobe analysis, using stoichiometric criteria. Mineral Mag 51:431-435

Evans BW, Frost BR (1975) Chrome-spinel in progressive metamorphism- a preliminary analysis. Geochim et Cosmochim Acta 39:959-972

Eslami A, Arai S, Miura M, Mackizadeh MA (2018) Metallogeny of the peridotite-hosted magnetite ores of the Nain ophiolite, Central Iran: Implications for Fe concentration processes during multi-episodic serpentinization. Ore Geol Rev 95:680-694

Fabriès J (1979) Spinel-olivine geothermometry in peridotites from ultramafic complexes. Contrib Mineral Petrol 69:329-336

Fiorentini ML, Stone WE, Beresford SW, Barley ME (2004) Platinum-group element alloy inclusions in chromites from Archaean mafic-ultramafic units: evidence from the Abitibi and the Agnew-Wiluna Greenstone Belts. Mineral and Petrol 82:341-355

Fleet ME, Angeli N, Pan Y (1993) Oriented chlorite lamellae in chromite from the Pedra Branca Mafic-Ultramafic Complex, Ceari, Brazil. Am Mineral 78:68-74

Fonseca ROC, Campbell IH, O'Neill HStC, Allen CM (2009) Solubility of Pt in sulphide mattes: Implications for the genesis of PGE-rich horizons in layered intrusions. Geochim et Cosmochim Acta 73:5764-5777

Gahlan HA, Arai S, Ahmed AH, Ishida Y, Abdel Aziz YM, Rahimi A (2006) Origin of magnetite veins in serpentinite from the Late Proterozoic Bou-Azzer ophiolite, Anti-Atlas, Morocco: An implication for mobility of iron during serpentinization. J Afr Earth Sci 46:318-330

Garuti G, Pushkarev E, Zaccarini F (2002) Composition and paragenesis of Pt alloys from chromitites of the Uralian-Alaskan type Kytlym and Uktus complexes, Northern and Central Urals, Russia. Canad Mineral 40:357-376

Gervilla F, Padrón-Navarta J, Kerestedjian T, Sergeeva I, González-Jiménez J, Fanlo I (2012) Formation of ferrian chromite in podiform chromitites from the Golyamo Kamenyane serpentinite, Eastern Rhodopes, SE Bulgaria: a two-stage process. Contrib Mineral Petrol 164:1-15

Gervilla F, Asta M, Fanlo I, Grolimund D, Sanchez DF, Samson V, Hunziker D, Colás V, González-Jiménez JM, Kerestedjian T, Sergeeva I (2019) Diffusion pathways of $Fe^{2+}$ and $Fe^{3+}$ during the formation of ferrian chromite: a µXANES study. Contrib Mineral Petrol 65:174-180

Godel B, Barnes SJ, Gürer D, Austin P, Fiorentini ML (2013) Chromite in komatiites: 3D morphologies with implications for crystallization mechanisms. Contrib Mineral Petrol 165:173-189

González-Jiménez JM, Kerestedjian T, Proenza-Fernández JA, Gervilla-Linares F (2009) Metamorphism on chromite ores from the Dobromirtsi ultramafic massif, Rhodope Mountains (SE Bulgaria). Geol Acta 7:413-429

González-Jiménez JM, Griffin WL, Proenza JA, Gervilla F, O’Reilly SY, Akbulut M, Pearson NJ, Arai S (2014) Chromitites in ophiolites: How, where, when, why? Part II. The crystallisation of chromitites. Lithos 189:140-158

Habtoor AM, Ahmed AH, Akizawa N, Harbi H, Arai S (2017) Chemical homogeneity of high-Cr chromitites as indicator for widespread invasion of boninitic melt in mantle peridotite of Bir Tuluha ophiolite, Northern Arabian Shield, Saudi Arabia. Ore Geol Rev 90:243-259

Horn I, Foley SF, Jackson SE, Jenner GA (1994) Experimentally determined partitioning of high field strength and selected transition elements between spinel and basaltic melt. Chem Geol 117:193-218

Irvine TN (1967) Chromian spinel as a petrogenetic indicator. Part II. Petrological applications. Can J Earth Sci 4:71-103

Kamenetsky VS, Crawford AJ and Meffre S (2001) Factors controlling chemistry of magmatic spinel: An empirical study of associated olivine, Cr-spinel and melt inclusions from primitive rocks. J Petrol 42:655-671

Kamenetsky VS, Park J-W, Mungall JE, Pushkarev EV, Ivanov AV, Kamenetsky M B, Yaxley GM (2015) Crystallization of platinum-group minerals from silicate melts: Evidence from Cr spinel-hosted inclusions in volcanic rocks. Geology 43:903-906

Kimball KL (1990) Effects of hydrothermal alteration on the compositions of chromian spinels. Contrib Mineral Petrol 105:337-346

Lepage LD (2003) ILMAT: an excel worksheet for ilmenite-magnetite geothermometry and geobarometry. Comput Geosci 29:673-678

Lindsley DH (1981) The crystal chemistry and structure of oxide minerals as exemplified by the Fe-Ti oxides. *In*: Rumble D (ed.) Oxide Minerals. Mineralogical Society of America, Rev Mineral 3:1-52

Locmelis M, Pearson NJ, Barnes SJ, Fiorentini ML (2011) Ruthenium in komatiitic chromite. Geochim et Cosmochim Acta 75:3645-3661

Locmelis M, Fiorentini ML, Barnes SJ, Hanski EJ, Kobussene AF (2018) Ruthenium in chromite as indicator for magmatic sulfide liquid equilibration in mafic-ultramafic systems. Ore Geol Rev 97:152-170

Loferski JP (1986) Petrology of metamorphosed chromite-bearing ultramafic rocks from the Red Lodge District. USGS Bull, Professional Paper 44

Merlini A, Grieco G, Diella V (2009) Ferritchromite and chromian-chlorite formation in mélange-hosted Kalkan chromitite (Southern Urals, Russia). Am. Min. 94 (10):1459-1467

Mondal SK, Ripley EM, Li C, Frei R (2006) The genesis of Archean chromitites from the Nuasahi and Sukinda massifs in the Singhbhum craton, India. Precambr Res 148:45-66

Mondal SK (2009) Chromite and PGE deposits of Mesoarchean ultramafic-mafic suites within the greenstone belts of the Singhbhum craton, India: implications for mantle heterogeneity and tectonic setting. J Geol Soc India 73:36-51

Mondal SK, Das E, Banerjee R, Reisberg L (2019a) Trace Element in Chromites of Komatiites from the Archean Gorumahishani Greenstone Belt, Singhbhum Craton (India). Goldschmidt 2019, Barcelona (Spain)

Mondal SK, Khatun S, Prichard HM, Satyanarayanan M, Kumar GR (2019b) Platinum-group element geochemistry of boninite-derived Mesoarchean chromitites and ultramafic-mafic cumulate rocks from the Sukinda Massif (Orissa, India). Ore Geol Rev 104:722-744

Mukherjee R, Mondal SK, Rosing MT, Frei R (2010) Compositional variations in the Mesoarchean chromites of the Nuggihalli schist belt, Western Dharwar Craton (India): potential parental melts and implication for tectonic setting. Contrib Mineral Petrol

160:865-885

Mukherjee R, Mondal SK, Gonzaléz-Jiménez JM, Griffin WL, Pearson, NJ, O’Reilly SY (2015) Trace element fingerprints of chromite, magnetite and sulfide from the 3.1 Ga ultramafic-mafic rocks of the Nuggihalli greenstone belt, Western Dharwar Craton (India). Contrib Mineral Petrol 169:1-23

Mukhopadhyay J, Beukes NJ, Armstrong RA, Zimmermann U, Ghosh G, Medda RA (2008) Dating the oldest Greenstone in India, a 3.51-Ga precise U–Pb SHRIMP zircon age for Dacitic Lava of the Southern Iron Ore Group, Singhbhum Craton. J Geol 116:449-461

Nell J, O'Neill HStC (1997) The Gibbs free energy of formation and heat capacity of ß-$Rh_2O_3$ and "$MgRh_2O_4$", the MgO-Rh-O phase diagram, and constraints on the stability of $Mg_2Rh^{4+}O_4$. Geochim et Cosmochim Acta 61:4159-4171

Nicklas RW, Puchtel IS, Ash RD (2016) High-precision determination of the oxidation state of komatiite lavas using vanadium liquid-mineral partitioning. Chem Geol 433:36-45

Nicklas RW, Puchtel IS, Ash RD, Piccoli PM, Hanski E, Nisbet EG, Waterton PM, Pearson DG, Anbar AD (2019) Secular mantle oxidation across the Archean Proterozoic boundary: evidence from V partitioning in komatiites and picrites. Geochim Cosmochim Acta 250:49-75

Pagé P, Barnes S-J (2009) Using trace elements in chromites to constrain the origin of podiform chromitites in the Thetford Mines ophiolite, Québec, Canada. Econ Geol 104:997-1018

Pagé P, Barnes S-J, Bédard JH, Zientek ML (2012) In situ determination of Os, Ir, and Ru in chromites formed from komatiite, tholeiite and boninite magmas: implications for chromite control of Os, Ir and Ru during partial melting and crystal fractionation. Chem Geol 302:3-15

Pagé P, Barnes S-J (2016) The influence of chromite on osmium, iridium, ruthenium and rhodium distribution during early magmatic processes. Chem Geol 420:51-68

Park J-W, Campbell IH, Eggins SM (2012) Enrichment of Rh, Ru, Ir and Os in Cr spinels from oxidized magmas: evidence from the Ambae volcano, Vanuatu. Geochim et Cosmochim Acta 78:28-50

Park J-W, Kamenetsky V, Campbell I, Park G, Hanski E, Pushkarev E (2017) Empirical constraints on partitioning of platinum group elements between Cr-spinel and primitive terrestrial magmas. Geochim Cosmochim Acta 216:393-416

Peach CL, Mathez EA (1996) Constraints on the formation of platinum-group element deposits in igneous rocks: Econ Geol 91:439-450

Prichard HM, Barnes S-J, Fisher PC, Pagé P, Zientek ML (2017) Laurite and associated PGM in the Stillwater Chromitites: Implications for processes of formation, and comparisons with laurite in the Bushveld and ophiolitic chromitites. Canad Mineral 55(1):121-144

Proenza JA, Ortega-Gutiérrez F, Camprubí A, Tritlla J, Elías-Herrera M, Reyes-Salas M (2004) Paleozoic serpentinite-enclosed chromitites from Tehuitzingo (Acatlán Complex, southern Mexico): a petrological and mineralogical study. J South Am Earth Sci 16:649-666

Proenza JA, Zaccarini F, Escayola M, Cábana C, Shalamuk A, Garuti G (2008) Composition and textures of chromite and platinum-group minerals in chromitites of the western ophiolitic belt from Córdoba Pampeans Ranges, Argentine. Ore Geol Rev 33:32-48

Puchtel IS, Humayun M, Campbell AJ, Sproule RA, Lesher CM (2004) Platinum group element geochemistry of komatiites from the Alexo and Pyke Hill areas, Ontario, Canada. Geochim et Cosmochim Acta 68(6):1361-1383

Righter K, Downs RT (2001) The crystal structures of synthetic Re- and PGE-bearing magnesioferrite spinels: Implications for impacts, accretion and the mantle. Geophys Res Lett 28:619-622

Righter K, Campbell AJ, Humayun M, Hervig RL (2004). Partitioning of Ru, Rh, Pd, Re, Ir, and Au between Cr-bearing spinel, olivine, pyroxene and silicate melts. Geochim et Cosmochim Acta 68:867-880

Righter K, Leeman WP, Hervig RL (2006) Partitioning of Ni, Co and V between spinel structured oxides and silicate melts: Importance of spinel composition. Chem Geol 227:1-25

Roeder PL, Campbell IH, Jamieson HE (1979) A re-evaluation of the olivine-spinel geothermometer. Contrib Mineral Petrol 68:325-334

Roeder PL (1994) Chromite: from the fiery rain of chondrules to the Kilauea Iki lava lake. Can Mineral 32:729-746

Sack, R. O. & Ghiorso, M. S. (1991). Chromian spinels as petrogenetic indicators: thermodynamic and petrological applications. Am. Mineral. 76, 827-847

Saha AK (1994) Crustal evolution of Singhbhum-North Orissa, eastern India. Geol Soc India 27:1-341

Sahu N K, Mukherjee MM (2001) Spinifex textured komatiite from Badampahar-Gorumahishani schist belt, Mayurbhanj District, Orissa. J Geol Soc India 57:529-534

Sattari P, Brenan JM, Horn I, McDonough WF (2002) Experimental constraints on the sulphide and chromite-silicate melt partitioning behaviour of rhenium and platinum-group elements. Econ Geol 97:385-398

Sievwright RH, O’Neill HSC, Tolley J, Wilkinson JJ, Berry AJ (2020) Diffusion and partition coefficients of minor and trace elements in magnetite as a function of oxygen fugacity at 1150 ºC. Contrib Mineral Petrol 175(5):1-21

Stowe CW (1997) Chromite deposits of the Shurugwi greenstone belt, Zimbabwe. In: Stowe CW (Ed), Evolution of Chromium Ore Fields. Hutchinson Ross publication, New York, pp 71-88

Törmänen T, Konnunaho JP, Hanski E, Moilanen M, Heikura P (2016) The Paleoproterozoic komatiite-hosted PGE mineralization at Lomalampi, Central Lapland Greenstone Belt, northern Finland. Miner Deposita 51:411-430

Tredoux M, Lindsay NM, Davies G, McDonald I (1995) The fractionation of platinum-group elements in magmatic systems, with the suggestion of a novel causal mechanism. S Afr J Geol 98:157-167

Wylie AG, Candela PA, Burke TM (1987) Compositional zoning in unusual Zn-rich chromite from the Sykesville district of Maryland and its bearing on the origin of “ferritchromit”. Am Min. 72 (3-4):413-422

Yadav PK, Pradhan UK, Mukherjee A, Sar RN, Sahoo P, Das M (2015) Basic characterization of Kapili komatiite from Badampahar-Gorumahishani schist belt, Singhbhum Craton, Odisha, India. Indian J Geosci 69:1-12

Yadav PK, Das M (2017) Geochemistry of Kapili komatiite from Badampahar-Gorumahishani greenstone belt, Singhbhum craton, India and its resemblance with ‘Barberton Komatiite’. Int j res Anal Rev 4:495-507

Yu H, Zhang H-F, Zou H-B, Yang Y-H (2019) Minor and trace element variations in chromite from the Songshugou dunites, North Qinling Orogen: Evidence for amphibolite-facies metamorphism. Lithos 328-329:146-158

Zhou M–F, Kerrich R (1992) Morphology and composition of chromite in komatiites from the Belingwe Greenstone Belt, Zimbabwe. Canad Mineral 30:303-317

## Figure captions

**Fig. 1** (***a***) Generalized geology of the Singhbhum Craton, India (after Saha 1994; Mondal et al. 2006). Inset map of India shows the location of the Singhbhum Craton. 1 - Singhbbum Granite Batholithic Complex, 2 - OMTG Tonalite-Granodiorite, 3 - OMG Supracrustals, 4 - Iron Ore Group greenstone sequences with BIF, 5 - Ultramafic-Mafic rocks with chromite-PGE deposits, 6 - Late Archean-Proterozoic sedimentary sequence, 7 - Late Archean-Proterozoic volcanic sequence. (***b***) Geological map of the Gorumahishani-Badampahar greenstone belt (modified from www.gsi.gov.in) showing the locations of Maharajgunj, Chuka Pahar, Tua Dungri, and Kapili komatiite hillocks. (***c***) Lithological column of Tua Dungri komatiite hill. The map in the right top corner shows the sample locations. (***d***) Geology of the Kapili area showing the sample locations. (***e***) Lithological column of the komatiitic suite of rocks from Maharajgunj and Chuka Pahar sections. The map in the middle shows the sample locations.

**Fig. 2** Field photographs: (***a***) Meta-dunite from Tua Dungri (lower cumulate zone), (***b***) Chevron spinifex-textured meta-peridotite from Kapili (spinifex zone), (***c***) Platy spinifex textured meta-peridotite from Tua Dungri (spinifex zone), (***d***) Random spinifex-textured meta-peridotite from Kapili (spinifex zone), (***e***) Schistose meta-basalt from Tiring, and (***f***) Quartzite band interlayered with schists from Kapili.

**Fig. 3** Photomicrographs of komatiitic rocks in transmitted and reflected light: (***a***) Small olivine (ol) core is surrounded by serpentine (srp) and associated with accessory chromite (chr), (***b***) Serpentine shows pseudomorphic texture (after olivine) with accessory chromite. Chlorite (chl) and tremolite (tr) form the interstitial assemblage, (***c***) Carbonate (cb) minerals in the meta-peridotite, (***d***) Spinifex texture now represented by tremolite after pyroxene grains. Magnetite is present in between tremolite grains, (***e***) Spinifex texture now represented by serpentine after olivine grains. An assemblage of chlorite + tremolite + carbonate is present in between serpentine spinifexes, (***f***) Meta-basalt contains epidote (ep) after plagioclase along with chlorite and tremolite, (***g***) Photomicrograph of type-IV fractured chromite grain and completely altered to ferritchromit (fcmt), (***h***) Backscattered electron (BSE) image of type-V small to large anhedral grains completely altered to chrome magnetite.

**Fig. 4** Comparison of modal abundances (in %) of mineral phases from the komatiitic suite of rocks between northern Maharajgunj, Chuka Pahar, Tua Dungri, and southern Kapili areas.

**Fig. 5** Quantitative microprobe profiles of major and minor element oxides along with Mg#, Cr#, and $Fe^{3+}/R^{3+}$ across the (***a***) Type-I (sample: MIC/16/39), (***b***) Type-II (sample: SHB/18/24), and (***c***) Type-III (sample: SHB/18/36) zoned chromite grains showing variation from chromite cores to ferritchromit and chrome magnetite rims.

**Fig. 6** Compositions of chromites from Gorumahishani komatiitic rocks: (***a***), (***b***) Mg# vs. Cr# and (***c***) Mg# vs. $Fe^{3+}/(Fe^{3+}+Cr+Al)$ variations of the type-I, II, III, IV, and, V Cr-spinels, (***d***), (***e***), (***f***) Variations of $Fe^{3+}/(Fe^{3+}+Cr+Al)$ plotted against $TiO_2$, MnO, and NiO from all types of Cr-spinels, (***g***) Cr, Al, and $Fe^{3+}$ variation of the type-I, II, III chromite cores, and rims along with type-IV and type-V grains.

**Fig. 7** Quantitative *in situ* LA-ICPMS profiles of trace and platinum-group elements along with major elements $Cr_2O_3$, $Al_2O_3$, MgO, $Fe_2O_3$, FeO and Mg#, Cr#, $Fe^{3+}/R^{3+}$ across the (***a***), (***b***) Type-I and (sample: MIC/16/39) (***c***), (***d***) Type- II (sample: SHB/19-12/82) zoned chromites. LA ponts: (***a***) Chr: 8, 9 and chrome magnetite: 7, 10; (***b***) Chr: 3, fcmt: 4, and chrome magnetite: 5; (***c***) Chr: 25, chrome magnetite: 26; (***d***) Chr: 34, chrome magnetite: 33. Laser spots indicate data points showing variation from chromite core to ferritchromit and chrome magnetite rims.

**Fig. 8** Compositional variations of the type-I, type-II, and type-V Cr-spinel grains from (***a***)-(***g***) Mg# vs. Ga, Ni, Sc, Co, Mn, Zn, and Ti plots, (***h***) Zn+Co+Mn vs. Ga plot.

**Fig. 9** EPR MORB Cr-spinel (after Pagé and Barnes 2009) normalized spidergrams: (***a***) Average major, and trace elements compositional variation of the type-I, type-II, and type-V Cr-spinels and (***b***) Comparison of type-I, type-II, and type-V Cr-spinels with the least altered chromites from Finland komatiite and Greenland, Troodos, and Kamchatka picrite (Park et al. 2017).

**Fig. 10** Representative time-resolved spectra of LA-ICPMS analyses on komatiitic chromites from (***a***) Sample MIC/16/39 (type-I chromite, Tua Dungri) showing homogenous PGE spectra (***b***) Sample SHB/19-12/35 (type-V chromite, Maharajgunj) with Rh, Ru spikes indicating the probable presence of Rh, Ru-bearing micro-inclusions.

**Fig. 11** Primitive mantle normalized Rh and IPGE plot of (*a*) Type- I, type-II, and type-V Cr-spinel grains from the Gorumahishani komatiitic rocks and (*b*) Comparison of type-I, type-II, and type-V Cr-spinels with the least altered chromites from Finland komatiite and Greenland, Troodos, Finland, Emeishan, and Kamchatka picrites (Park et al. 2017). Primitive mantle values are from Barnes et al. (1988).

**Fig. 12** Compositional variations of trace and platinum-group elements in the type-I, type-II, and type-V Cr-spinel grains. (***a***) V vs. Ru. (***b***) Ni vs. Ru.

**Fig. 13** Schematic illustration of microstructural and chemical (major, minor, and trace element along with IPGE, Rh) changes in the five types of Cr-spinel grains during progressive metamorphism of komatiitic rocks from the Gorumahishani greenstone belt.

## Table captions

**Table 1** Classification of komatiitic chromites from the Gorumahishani greenstone belt.

**Table 2** Major and minor element compositional ranges of the Cr-spinels (wt.%)

**Table 3** Trace element compositional range of the Cr-spinels (ppm) measured by LA-ICP-MS.

**Table 4** Platinum-group element (PGE) compositional range of the Cr-spinels (ppb) measured by LA-ICP-MS.

**Table 5** Empirical partition coefficients of trace elements ($D^{\text{Cr-spinel/silicate melt}}$).

**Table 6** Empirical partition coefficients of IPGEs and Rh ($D^{\text{Cr-spinel/ilicate melt}}$).

## Supplementary materials

**Appendix 1:** Detailed information on the geological background of the Singhbhum craton and analytical methods

**Appendix 2:** Supplementary figures

Fig. S1 (a) Classification of pyroxene (after Morimoto 1988), (b) amphibole (after Leake et al. 1997), (c) carbonate, and (d) chlorite (after Hey 1954) from the komatiitic suite of rocks from the Gorumahishani greenstone belt.

Fig. S2 Compositional variations of the type-I, type-II, and type-V chromite grains in $Al_2O_3$ vs. Ga plots.

Fig. S3 Variation in platinum-group elements concentration (in ppb) of the type-V chrome magnetite grains from the northern and southern part of the Gorumahisani greenstone belt.

**Appendix 3:** Complete set of analytical data

Table S1 Major and minor element analyses of the silicate and carbonate minerals (wt.%).

Table S2 Major and minor EMPA analyses of the oxide minerals (wt.%).

Table S3 Trace element LA-ICPMS analyses of the oxide minerals (ppm).

Table S4 Platinum-group element LA-ICPMS analyses of the oxide minerals (ppb).

Table S5 Whole-rock major element (wt.%), trace element (ppm), and platinum-group element (PGE) (ppb) compositions of selected samples.

Table S6 Empirical partition coefficients of trace elements ($D^{Cr\text{-}spinel/silicate\ melt}$). Calculated results also shown for mass fractions of chromite in komatiitic rocks,contribution of chromite to the whole rock budget of each element, silicate melt concentrations for each element.

Table S7 Empirical partition coefficients of platinum-group elements ($D^{Cr\text{-}spinel/silicate\ melt}$). Calculated results also shown for mass fractions of chromite in komatiitic rocks, contribution of chromite to the whole rock budget of each element, silicate melt concentrations for each element.

Figure 01

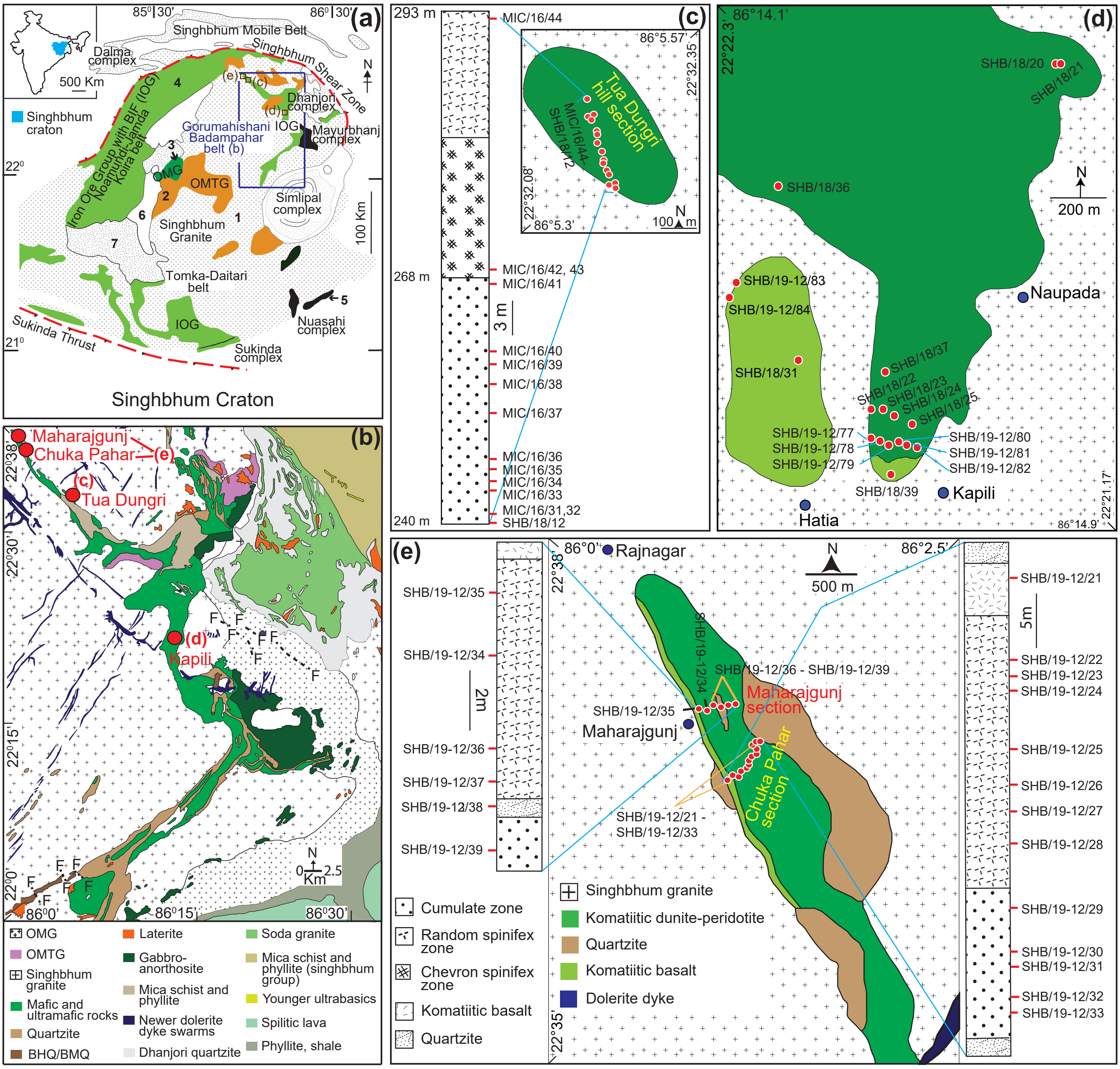
(a)
85°30'
86°30'
Singhbhum Mobile Belt
Dalma complex
500 Km
Singhbhum craton
Singhbhum Shear Zone
N
(e)
(c)
(d)
Dhanjori complex
Mayurbhanj complex
IOG
Gorumahishani Badampahar belt (b)
Iron Ore Group with BIF (IOG) Noamundi-Jamda Koira belt
4
3
OMG
OMTG
2
6
1
7
Simlipal complex
Singhbhum Granite
100 Km
22°
Tomka-Daitari belt
5
Nuasahi complex
IOG
Sukinda Thrust
Sukinda complex
21°
Singhbhum Craton
(b)
Maharajgunj
Chuka Pahar
(e)
(c)
Tua Dungri
(d)
Kapili
22°38'
22°30'
22°15'
22°0'
86°0'
86°15'
86°30'
N
0 2.5 Km
F
OMG
OMTG
Singhbhum granite
Mafic and ultramafic rocks
Quartzite
BHQ/BMQ
Laterite
Gabbro-anorthosite
Mica schist and phyllite
Newer dolerite dyke swarms
Dhanjori quartzite
Soda granite
Mica schist and phyllite (singhbhum group)
Younger ultrabasics
Spilitic lava
Phyllite, shale
(c)
293 m
268 m
240 m
3 m
MIC/16/44
MIC/16/42, 43
MIC/16/41
MIC/16/40
MIC/16/39
MIC/16/38
MIC/16/37
MIC/16/36
MIC/16/35
MIC/16/34
MIC/16/33
MIC/16/31,32
SHB/18/12
86°5.57'
22°32.35'
22°32.08'
86°5.3'
Tua Dungri hill section
MIC/16/44-SHB/18/12
N
100 m
(d)
86°14.1'
22°22.3'
SHB/18/20
SHB/18/21
SHB/18/36
N
200 m
SHB/19-12/83
SHB/19-12/84
Naupada
SHB/18/31
SHB/18/37
SHB/18/22
SHB/18/23
SHB/18/24
SHB/18/25
SHB/19-12/77
SHB/19-12/78
SHB/19-12/79
SHB/19-12/80
SHB/19-12/81
SHB/19-12/82
SHB/18/39
Kapili
Hatia
22°21.17'
86°14.9'
(e)
SHB/19-12/35
SHB/19-12/34
2m
SHB/19-12/36
SHB/19-12/37
SHB/19-12/38
SHB/19-12/39
86°0''
Rajnagar
86°2.5'
22°38'
N
500 m
SHB/19-12/34
SHB/19-12/36 - SHB/19-12/39
Maharajgunj section
SHB/19-12/35
Maharajgunj
Chuka Pahar section
SHB/19-12/21 - SHB/19-12/33
22°35'
SHB/19-12/21
5m
SHB/19-12/22
SHB/19-12/23
SHB/19-12/24
SHB/19-12/25
SHB/19-12/26
SHB/19-12/27
SHB/19-12/28
SHB/19-12/29
SHB/19-12/30
SHB/19-12/31
SHB/19-12/32
SHB/19-12/33
Cumulate zone
Random spinifex zone
Chevron spinifex zone
Komatiitic basalt
Quartzite
Singhbhum granite
Komatiitic dunite-peridotite
Quartzite
Komatiitic basalt
Dolerite dyke

Figure 02

Figure 03

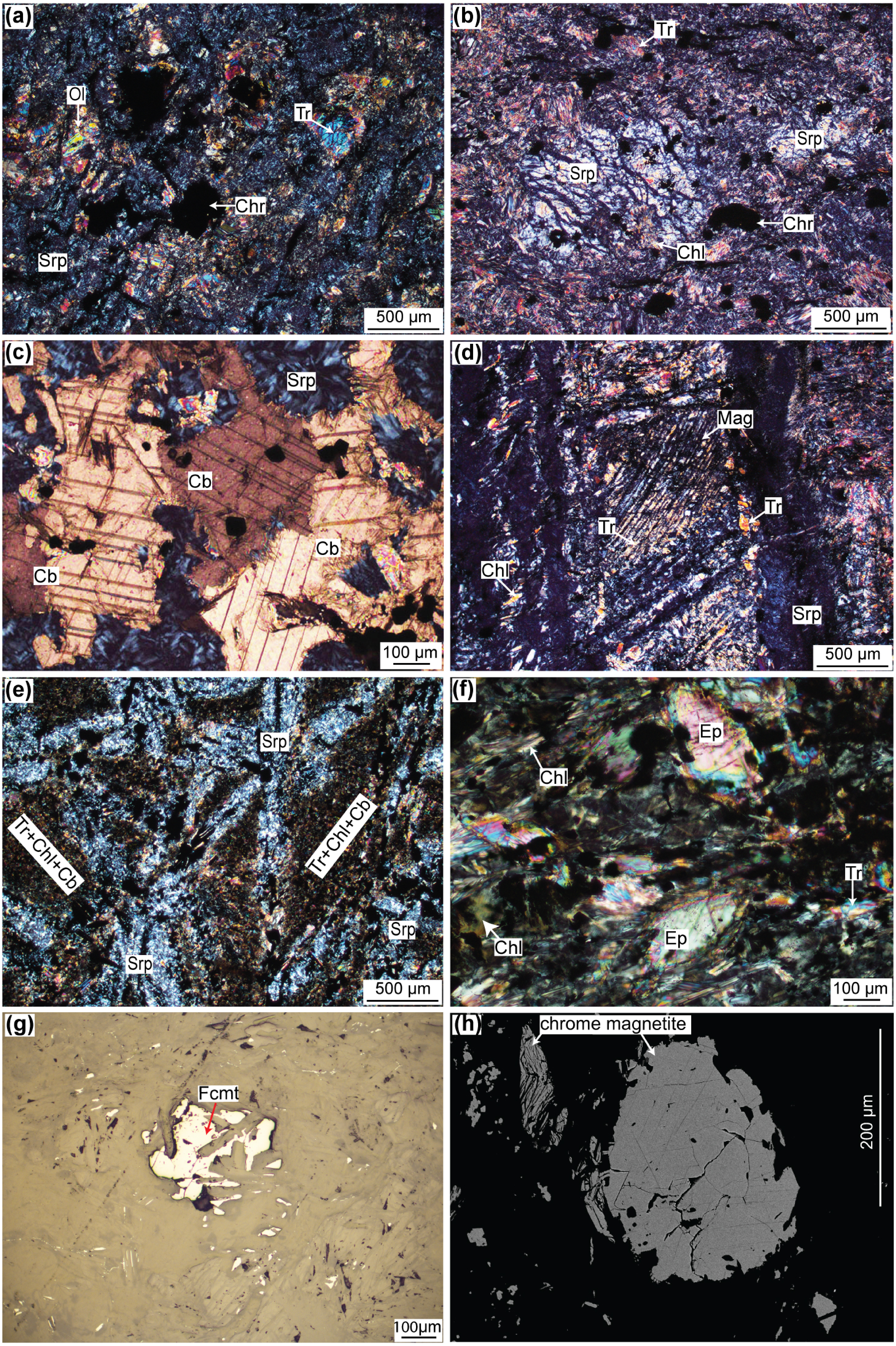
(a)
Ol
Tr
Chr
Srp
500 μm
(b)
Tr
Srp
Srp
Chr
Chl
500 μm
(c)
Srp
Cb
Cb
Cb
100 μm
(d)
Mag
Tr
Tr
Chl
Srp
500 μm
(e)
Srp
Tr+Chl+Cb
Tr+Chl+Cb
Srp
Srp
500 μm
(f)
Ep
Chl
Tr
Chl
Ep
100 μm
(g)
Fcmt
100μm
(h)
chrome magnetite
200 μm

Figure 04

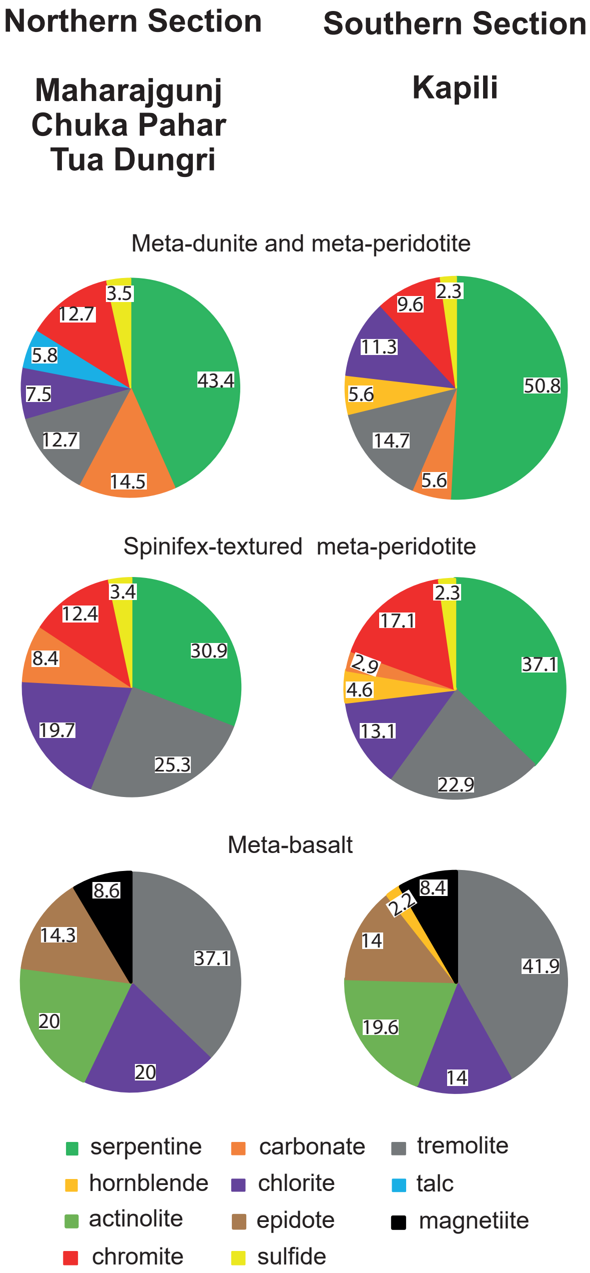
Northern Section
Southern Section
Maharajgunj
Chuka Pahar
Tua Dungri
Kapili
Meta-dunite and meta-peridotite
3.5
12.7
5.8
7.5
12.7
14.5
43.4
2.3
9.6
11.3
5.6
14.7
5.6
50.8
Spinifex-textured meta-peridotite
3.4
12.4
8.4
19.7
25.3
30.9
2.3
17.1
2.9
4.6
13.1
22.9
37.1
Meta-basalt
8.6
14.3
20
20
37.1
8.4
2.2
14
19.6
14
41.9
serpentine
carbonate
tremolite
hornblende
chlorite
talc
actinolite
epidote
magnetiite
chromite
sulfide

Figure 05

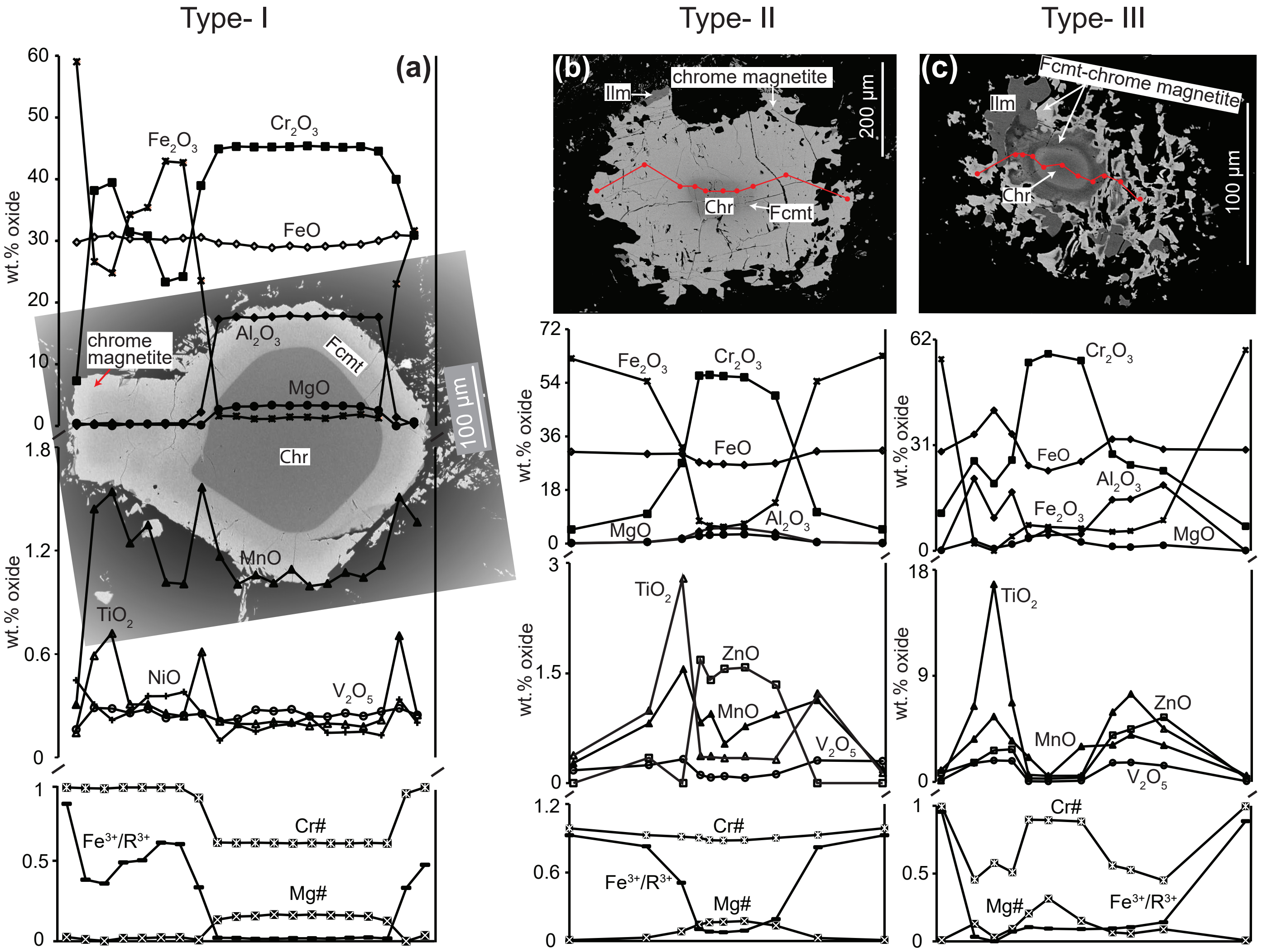
Type- I
Type- II
Type- III
(a)
(b)
(c)
wt.% oxide
60
50
40
30
20
10
0
1.8
1.2
0.6
0
1
0.5
0
Fe2O3
Cr2O3
FeO
Al2O3
MgO
chrome magnetite
Fcmt
Chr
100 µm
MnO
TiO2
NiO
V2O5
Cr#
Fe3+/R3+
Mg#
Ilm
chrome magnetite
200 µm
Chr
Fcmt
72
54
36
18
0
3
1.5
0
1.2
0.6
0
Fe2O3
Cr2O3
FeO
MgO
Al2O3
TiO2
ZnO
MnO
V2O5
Cr#
Fe3+/R3+
Mg#
Fcmt-chrome magnetite
Ilm
Chr
100 µm
62
31
0
18
9
0
1
0.5
0
Cr2O3
FeO
Al2O3
Fe2O3
MgO
TiO2
ZnO
MnO
V2O5
Cr#
Mg#
Fe3+/R3+

Figure 06

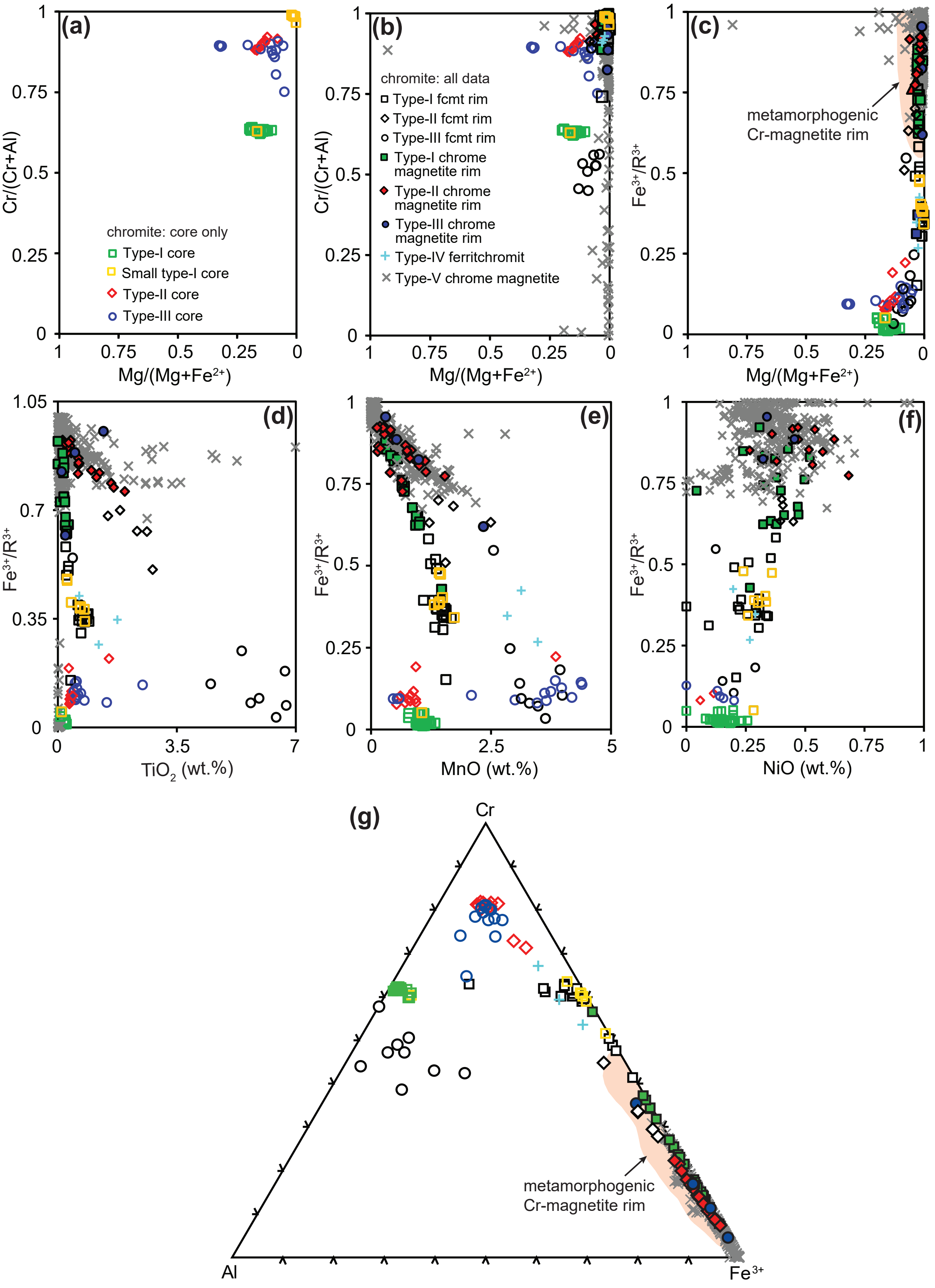
(a)
Cr/(Cr+Al)
Mg/(Mg+Fe$^{2+}$)
chromite: core only
Type-I core
Small type-I core
Type-II core
Type-III core
(b)
Cr/(Cr+Al)
Mg/(Mg+Fe$^{2+}$)
chromite: all data
Type-I fcmt rim
Type-II fcmt rim
Type-III fcmt rim
Type-I chrome magnetite rim
Type-II chrome magnetite rim
Type-III chrome magnetite rim
Type-IV ferritchromit
Type-V chrome magnetite
(c)
Fe$^{3+}$/R$^{3+}$
Mg/(Mg+Fe$^{2+}$)
metamorphogenic Cr-magnetite rim
1
0.75
0.5
0.25
0
(d)
Fe$^{3+}$/R$^{3+}$
TiO$_2$ (wt.%)
1.05
0.7
0.35
0
3.5
7
(e)
Fe$^{3+}$/R$^{3+}$
MnO (wt.%)
2.5
5
(f)
Fe$^{3+}$/R$^{3+}$
NiO (wt.%)
(g)
Cr
Al
Fe$^{3+}$
metamorphogenic Cr-magnetite rim

Figure 07

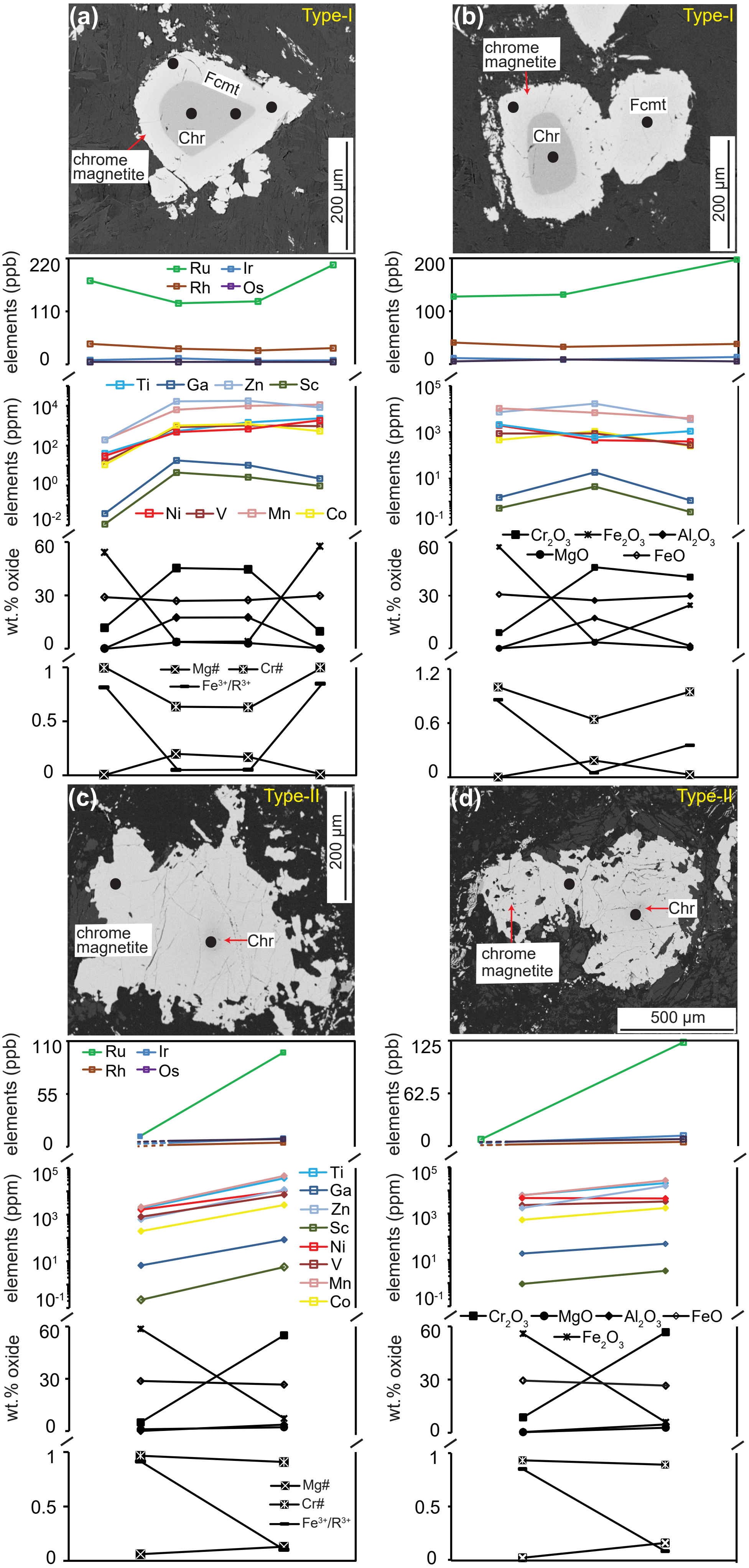
(a)
Type-I
Fcmt
Chr
chrome magnetite
200 μm
(b)
Type-I
chrome magnetite
Fcmt
Chr
200 μm
elements (ppb)
220
110
0
Ru
Ir
Rh
Os
200
100
0
elements (ppm)
$10^4$
$10^2$
$10^0$
$10^{-2}$
Ti
Ga
Zn
Sc
Ni
V
Mn
Co
$10^5$
$10^3$
$10^1$
$10^{-1}$
wt.% oxide
60
30
0
$Cr_2O_3$
$Fe_2O_3$
$Al_2O_3$
MgO
FeO
1
0.5
0
Mg#
Cr#
$Fe^{3+}/R^{3+}$
1.2
0.6
0
(c)
Type-II
200 μm
chrome magnetite
Chr
(d)
Type-II
Chr
chrome magnetite
500 μm
110
55
0
125
62.5
0
Ru
Ir
Rh
Os
Ti
Ga
Zn
Sc
Ni
V
Mn
Co
$Cr_2O_3$
MgO
$Al_2O_3$
FeO
$Fe_2O_3$
Mg#
Cr#
$Fe^{3+}/R^{3+}$

Figure 08

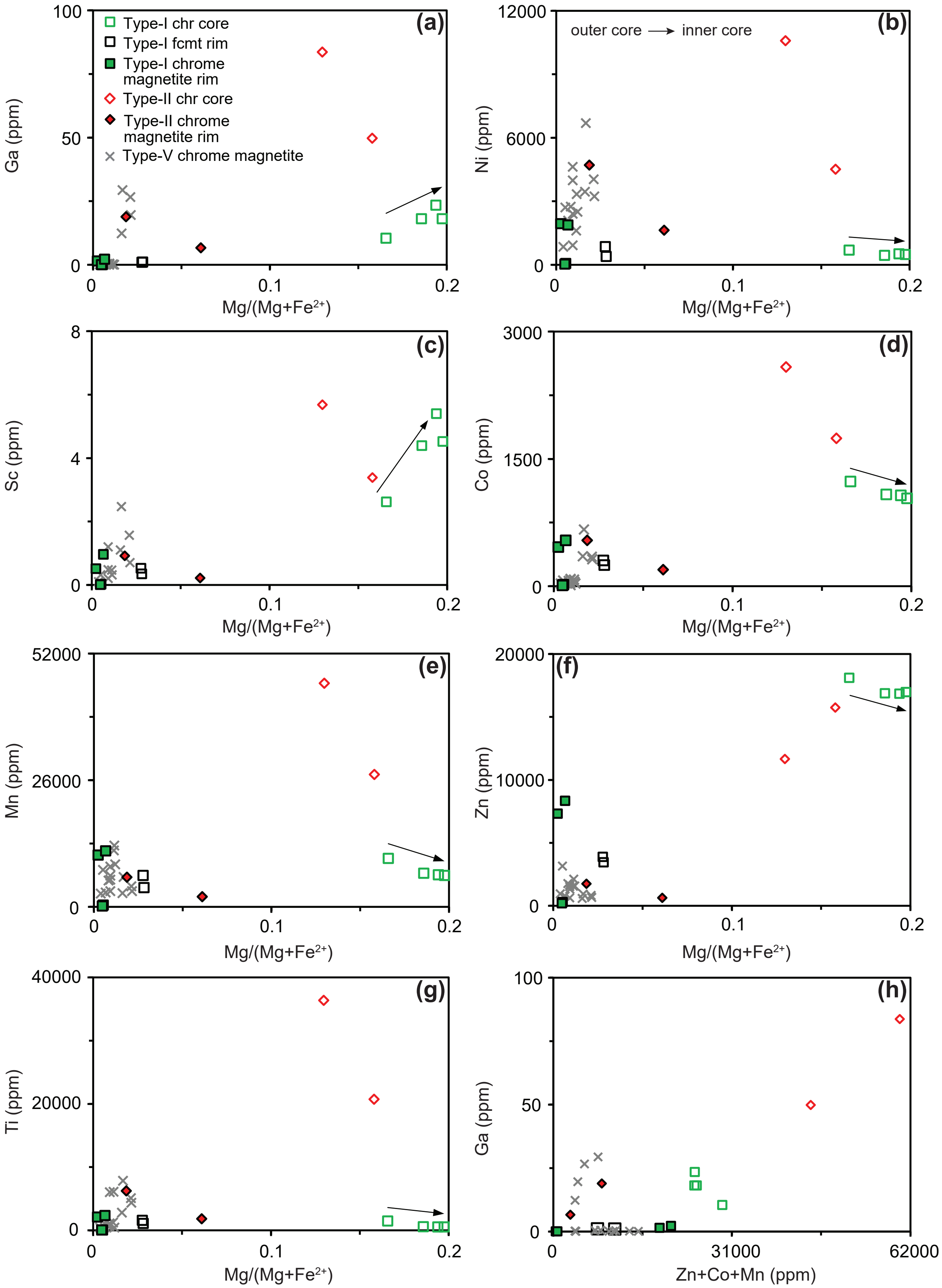
(a)
Ga (ppm)
100
50
0
0
0.1
0.2
Mg/(Mg+Fe$^{2+}$)
Type-I chr core
Type-I fcmt rim
Type-I chrome magnetite rim
Type-II chr core
Type-II chrome magnetite rim
Type-V chrome magnetite
(b)
outer core → inner core
Ni (ppm)
12000
6000
0
0
0.1
0.2
Mg/(Mg+Fe$^{2+}$)
(c)
Sc (ppm)
8
4
0
0
0.1
0.2
Mg/(Mg+Fe$^{2+}$)
(d)
Co (ppm)
3000
1500
0
0
0.1
0.2
Mg/(Mg+Fe$^{2+}$)
(e)
Mn (ppm)
52000
26000
0
0
0.1
0.2
Mg/(Mg+Fe$^{2+}$)
(f)
Zn (ppm)
20000
10000
0
0
0.1
0.2
Mg/(Mg+Fe$^{2+}$)
(g)
Ti (ppm)
40000
20000
0
0
0.1
0.2
Mg/(Mg+Fe$^{2+}$)
(h)
Ga (ppm)
100
50
0
0
31000
62000
Zn+Co+Mn (ppm)

Figure 09

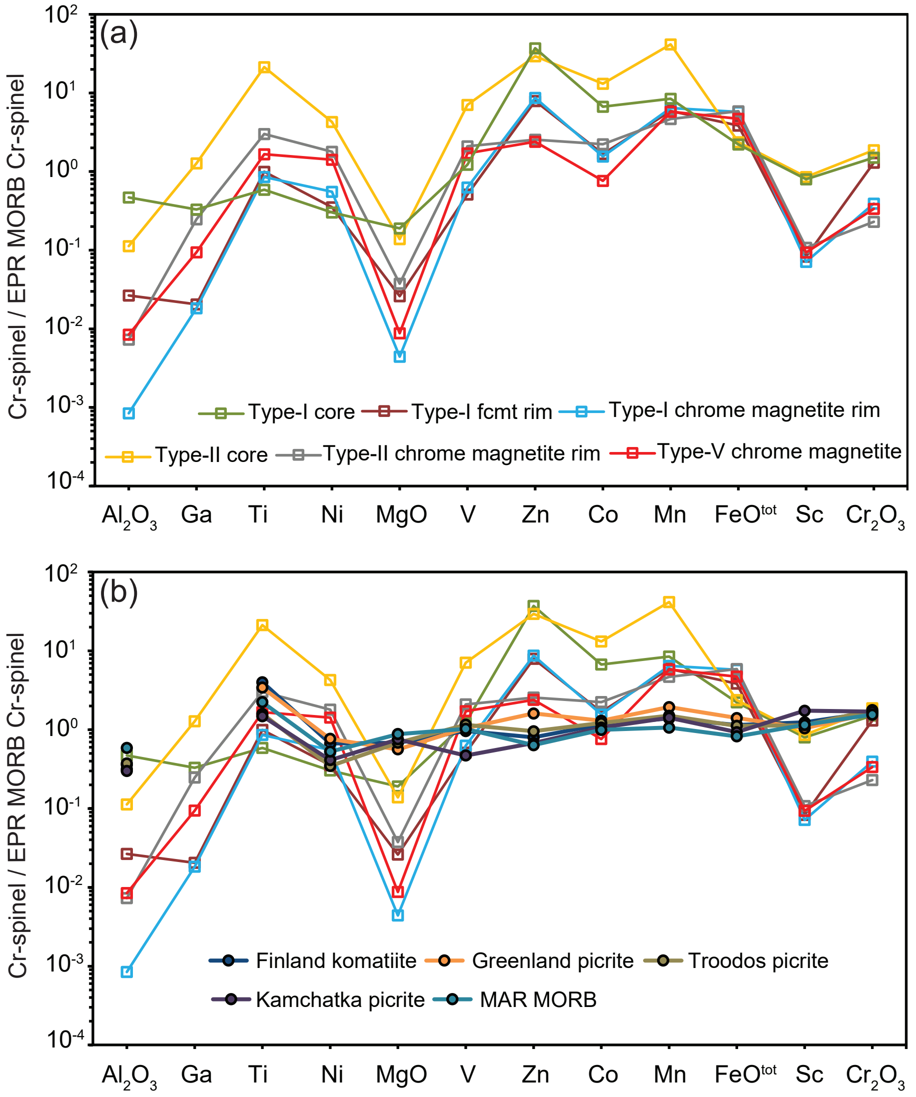
(a)
(b)
Cr-spinel / EPR MORB Cr-spinel
$10^{2}$
$10^{1}$
$10^{0}$
$10^{-1}$
$10^{-2}$
$10^{-3}$
$10^{-4}$
$Al_2O_3$
Ga
Ti
Ni
MgO
V
Zn
Co
Mn
$FeO^{tot}$
Sc
$Cr_2O_3$
Type-I core
Type-I fcmt rim
Type-I chrome magnetite rim
Type-II core
Type-II chrome magnetite rim
Type-V chrome magnetite
Finland komatiite
Greenland picrite
Troodos picrite
Kamchatka picrite
MAR MORB

Figure 10

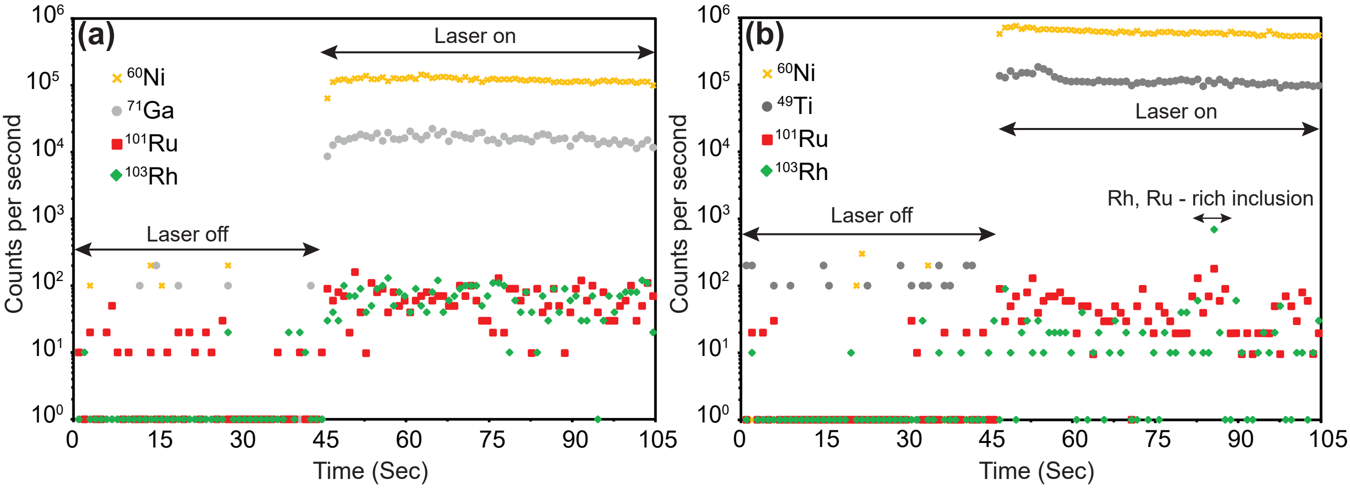

(a)
$^{60}$Ni
$^{71}$Ga
$^{101}$Ru
$^{103}$Rh
Laser on
Laser off
Counts per second
$10^0$
$10^1$
$10^2$
$10^3$
$10^4$
$10^5$
$10^6$
0
15
30
45
60
75
90
105
Time (Sec)
(b)
$^{60}$Ni
$^{49}$Ti
$^{101}$Ru
$^{103}$Rh
Laser on
Laser off
Rh, Ru - rich inclusion
Counts per second
Time (Sec)

Figure 11

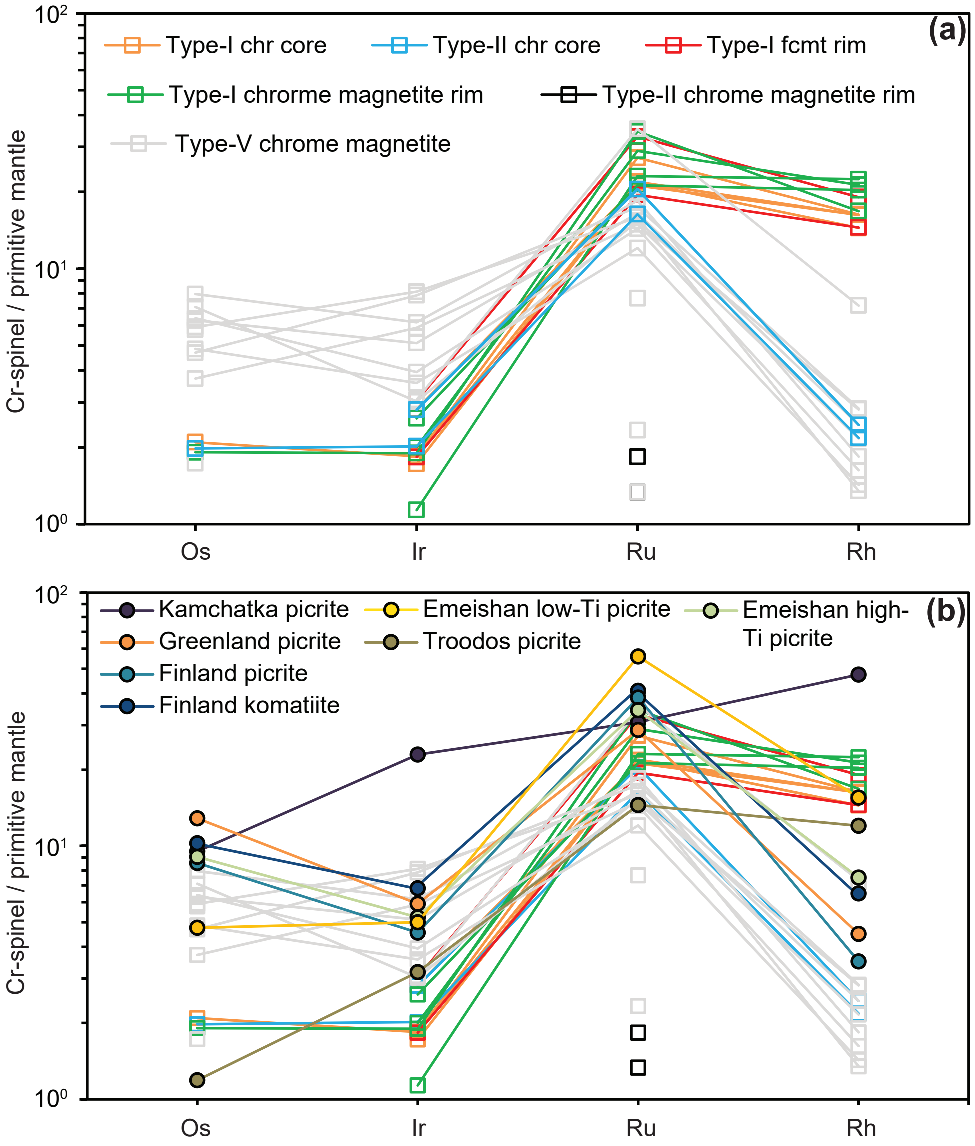
(a)
Type-I chr core
Type-II chr core
Type-I fcmt rim
Type-I chrorme magnetite rim
Type-II chrome magnetite rim
Type-V chrome magnetite
Cr-spinel / primitive mantle
$10^2$
$10^1$
$10^0$
Os
Ir
Ru
Rh
(b)
Kamchatka picrite
Emeishan low-Ti picrite
Emeishan high-Ti picrite
Greenland picrite
Troodos picrite
Finland picrite
Finland komatiite
Cr-spinel / primitive mantle
$10^2$
$10^1$
$10^0$
Os
Ir
Ru
Rh

Figure 12

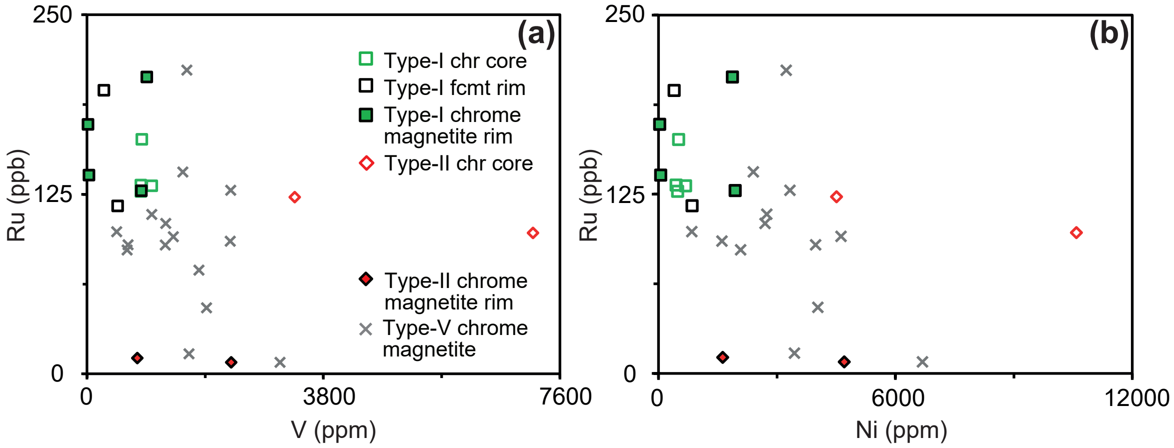
(a)
(b)
Type-I chr core
Type-I fcmt rim
Type-I chrome magnetite rim
Type-II chr core
Type-II chrome magnetite rim
Type-V chrome magnetite
250
125
0
Ru (ppb)
0
3800
7600
V (ppm)
0
6000
12000
Ni (ppm)

Figure 13

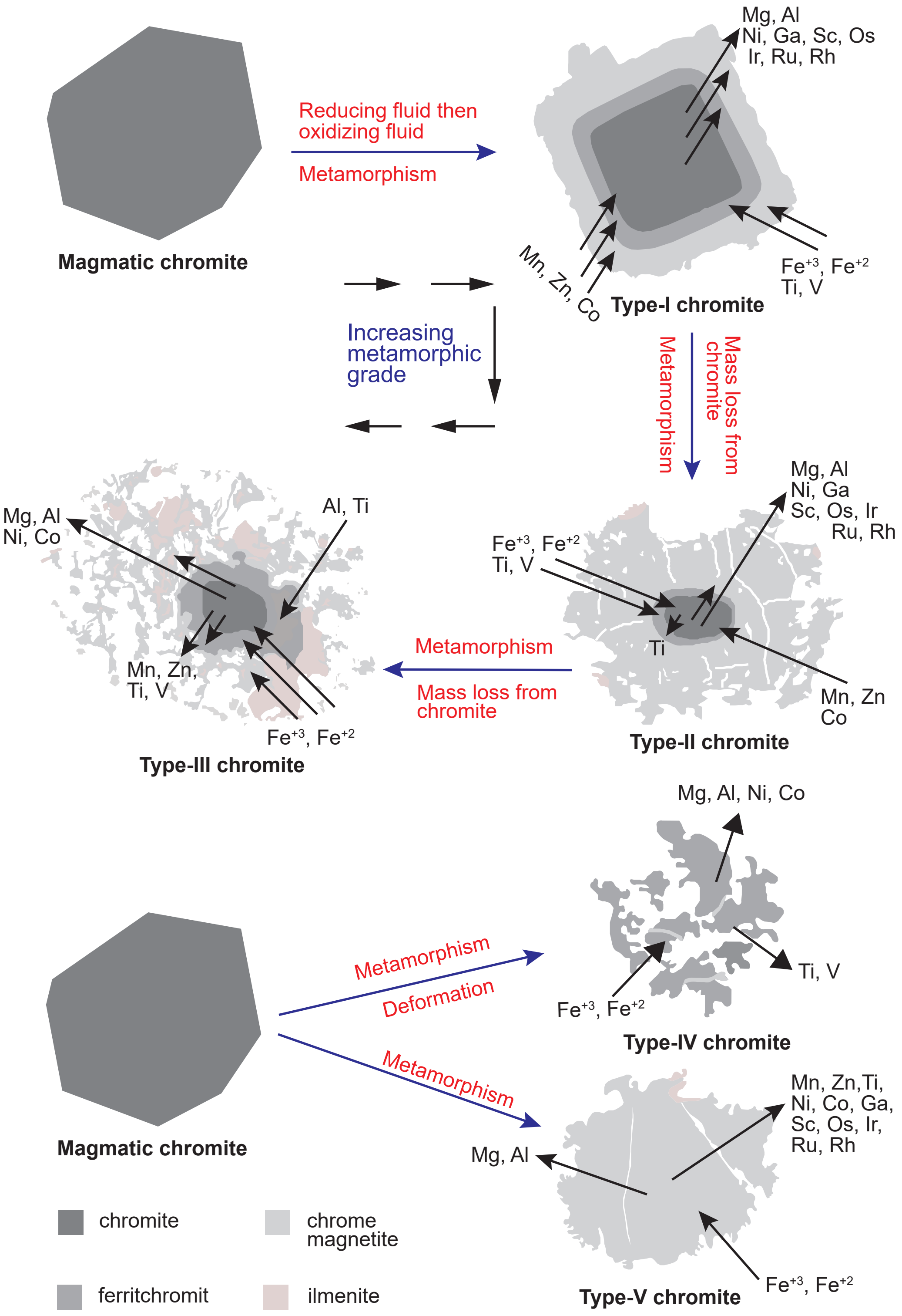
Magmatic chromite
Reducing fluid then oxidizing fluid
Metamorphism
Mg, Al
Ni, Ga, Sc, Os
Ir, Ru, Rh
Mn, Zn, Co
Fe$^{+3}$, Fe$^{+2}$
Ti, V
Type-I chromite
Increasing metamorphic grade
Metamorphism
Mass loss from chromite
Mg, Al
Ni, Ga
Sc, Os, Ir
Ru, Rh
Fe$^{+3}$, Fe$^{+2}$
Ti, V
Ti
Mn, Zn
Co
Type-II chromite
Metamorphism
Mass loss from chromite
Mg, Al
Ni, Co
Al, Ti
Mn, Zn,
Ti, V
Fe$^{+3}$, Fe$^{+2}$
Type-III chromite
Mg, Al, Ni, Co
Metamorphism
Deformation
Ti, V
Fe$^{+3}$, Fe$^{+2}$
Type-IV chromite
Metamorphism
Magmatic chromite
Mn, Zn,Ti,
Ni, Co, Ga,
Sc, Os, Ir,
Ru, Rh
Mg, Al
Fe$^{+3}$, Fe$^{+2}$
Type-V chromite
chromite
chrome magnetite
ferritchromit
ilmenite

**Table 1: Classification of komatiitic chromites from the Gorumahishani greenstone belt**

| Types of chromite | Study area | Host rock | Grain size | Textural and mineralogical character |
|---|---|---|---|---|
| **Type-I** | Tua Dungri | meta-dunite, meta-peridotite | ~400 - 530 µm × ~350 - 390 µm | Subhedral grain; non-porous low reflectance core and high reflectance ferritchromit to chrome magnetite rim with a sharp contact in between |
| **Type-II** | Southern part of Kapili | spinifex-textured meta-peridotite | ~550 - 620 µm × ~480 - 510 µm | Subhedral grain; low reflectance non-porous core with high reflectance thin ferritchromit rim, and wider, less porous chrome magnetite rim. Diffused contact in between cores and rims |
| **Type-III** | Northern part of Kapili | spinifex-textured meta-peridotite | ~255 - 268 µm × ~125 - 160 µm | Subhedral to anhedral grain; low and high reflectance inner rims with extensively porous outer chrome-magnetite envelope. Diffused contact in between cores and rims |
| **Type-IV** | Maharajgunj | meta-dunite, meta-peridotite | ~30 - 50 µm × ~70 - 100 µm | Anhedral grain; small fractured ferritchromit with almost homogeneous character. Occasionally, thin high reflectance magnetite rims are observed along the fracture planes |
| **Type-V** | Maharajgunj, Chuka Pahar, Tua Dungri, Kapili | meta-peridotite, spinifex-textured meta-peridotite, meta-basalt | ~40 - 60 µm × ~25 - 50 µm | Subhedral to euhedral grain. Optically and compositionally homogenous chrome-magnetite and magnetite with non-porous character |

**Table 2: EPMA major and minor elements compositional range (wt%) of komatiitic chromites from the Gorumahishani greenstone belt**

| **Location** | **TD** | **TD** | **KL** | **KL** | **TD** | **KL** | **KL** | **TD** | **KL** | **KL** | **MG** | **All** |
|---|---|---|---|---|---|---|---|---|---|---|---|---|
| **Mineral** | **Chr** | **Chr** | **Chr** | **Chr** | **Fcmt** | **Fcmt** | **Al rich Chr** | **Chr mag** | **Chr mag** | **Chr mag** | **Fcmt** | **Chr mag** |
| **Type** | **T-I Core** | **S T-I core** | **T-II core** | **T-III core** | **T-I R1** | **T- II R1** | **T-III R1** | **T-I R2** | **T-II R2** | **T-III R2** | **T-IV** | **Type-V** |
| **Data (n)** | **36** | **8** | **11** | **13** | **22** | **5** | **8** | **25** | **16** | **5** | **3** | **21** |
| **wt.%** | | | | | | | | | | | | |
| **$Al_2O_3$** | 17.23-18.38 | 0.23-0.96 | 2.8-5.16 | 3.55-9.14 | 0.15-9.95 | 0.88-1.72 | 12.65-21.15 | 0-0.19 | 0.03-0.71 | 0.01-1.09 | 1.74-2.56 | 0-1.61 |
| **MnO** | 0.78-1.25 | 1.41-1.74 | 0.54-3.85 | 0.47-4.4 | 1.1-1.68 | 1.41-2.50 | 2.90-3.99 | 0.13-1.02 | 0.19-1.54 | 0.31-2.35 | 2.84-3.48 | 0-2.8 |
| **TiO2** | 0.08-0.25 | 0.26-0.79 | 0.32-1.51 | 0.47-2.5 | 0.23-0.92 | 1.47-2.79 | 4.50-7.46 | 0-0.31 | 0.13-1.65 | 0.11-1.34 | 0.63-1.75 | 0-7.67 |
| **$Cr_2O_3$** | 44.45-46.84 | 33.04-44.62 | 45.59-56.79 | 41.19-58.06 | 26.89-42.54 | 16.92-27.03 | 23.47-28.96 | 5.03-24.20 | 4.69-13.26 | 2.83-22.73 | 34.2-42.1 | 0.92-19.57 |
| **MgO** | 2-3.75 | 0.04-0.35 | 1.25-3.13 | 0.84-6.24 | 0-0.68 | 0.51-1.55 | 0.81-2.86 | 0.04-0.52 | 0.15-1.05 | 0.13-0.18 | 0.32-0.54 | 0.02-5.68 |
| **$SiO_2$** | 0.09-0.30 | 0.23-0.27 | 0.08-0.17 | 0.05-0.15 | 0.08-1.46 | 0-0.04 | 0.03-0.12 | 0-0.47 | 0-0.77 | 0.07-0.12 | 0 .03-0.12 | 0-4.45 |
| **$Fe_2O_3$** | 0.84-4.04 | 22.96-32.24 | 5.54-14.94 | 6.2-10.82 | 26.89-42.54 | 32.26-44.71 | 2.1-14.88 | 41.8-62.28 | 50.15-63.03 | 41.63-62.62 | 17.61-28.47 | 42.79-66.14 |
| **FeO** | 26.42-30.65 | 29.80-30.94 | 25.51-27.62 | 22.91-27.91 | 29.25-31.29 | 28.33-30.33 | 29.8-34.26 | 29.17-30.55 | 28.76-31.25 | 27.9-31.57 | 27.68-29.02 | 27.06-34.03 |
| **$V_2O_3$** | 0.12-0.29 | 0.24-0.30 | 0.05-0.16 | 0.03-0.67 | 0.08-0.3 | 0.33-0.37 | 1.23-1.79 | 0.05-0.28 | 0.17-0.33 | 0.05-0.24 | 0.55-0.92 | 0-0.54 |
| **NiO** | 0-0.28 | 0.24-0.34 | 0.06-0.12 | 0-0.16 | 0-0.38 | 0.4-0.45 | 0.15-0.29 | 0.04-0.52 | 0.27-0.68 | 0.32-0.46 | 0.2-0.29 | 0-0.71 |
| **ZnO** | 1.63-2.11 | 0 | 1-2.41 | 0.28-3.03 | 0.52-0.88 | 0-1.45 | 1.64-5.48 | 0-0.38 | 0-0.63 | 0-1.16 | 1.29-1.61 | 0-0.62 |
| **CoO** | 0.02-0.23 | 0 | 0 | 0.02-0.23 | 0-0.16 | 0.12-0.27 | 0-0.32 | 0-0.14 | 0-0.16 | 0-0.07 | 0-0.11 | 0-0.31 |
| **Cation** | | | | | | | | | | | | |
| **Al** | 5.387-5.867 | 0.084-0.343 | 0.989-1.747 | 1.231-3.108 | 0.055-3.408 | 0.323-0.618 | 4.260-6.617 | 0-0.067 | 0.010-0.223 | 0.005-0.397 | 0.623-0.908 | 0-0.589 |
| **Mn** | 0.175-0.311 | 0.365-0.446 | 0.130-0.976 | 0.110-1.092 | 0.280-0.431 | 0.313-0.654 | 0.702-0.952 | 0.034-0.263 | 0.049-0.400 | 0.080-0.616 | 0.736-0.885 | 0-0.750 |
| **Ti** | 0.017-0.061 | 0.022-0.181 | 0.070-0.339 | 0.107-0.541 | 0.053-0.208 | 0.347-0.637 | 0.936-1.581 | 0-0.072 | 0.031-0.379 | 0.025-0.311 | 0.143-0.402 | 0-1.825 |
| **Cr** | 9.456-9.651 | 8.026-9.735 | 10.783-12.882 | 9.396-12.718 | 6.456-9.780 | 4.146-6.499 | 5.138-6.350 | 1.249-5.786 | 1.153-3.214 | 0.689-5.575 | 8.193-10.004 | 0.231-4.829 |
| **Mg** | 0.820-1.484 | 0.019-1.159 | 0.559-1.333 | 0.360-2.575 | 0.002-0.310 | 0.233-0.701 | 0.343-1.132 | 0.020-0.236 | 0.068-0.494 | 0.059-0.082 | 0.145-0.248 | 0.009-2.517 |
| **Si** | 0.026-0.081 | 0.071-0.084 | 0.019-0.050 | 0.015-0.042 | 0.024-0.447 | 0-0.013 | 0.008-0.020 | 0-0.148 | 0-0.242 | 0.022-0.036 | 0.008-0.038 | 0-1.323 |
| **$Fe^{3+}$** | 5.238-7.452 | 0.764-7.452 | 1.198-3.364 | 1.361-2.343 | 2.366-9.067 | 7.385-10.431 | 0.420-3.198 | 9.683-14.713 | 11.575-14.584 | 9.719-14.530 | 3.983-6.493 | 9.803-15.624 |
| **$Fe^{2+}$** | 7.655-7.843 | 5.978-7.935 | 6.296-6.763 | 5.304-6.735 | 7.341-7.923 | 7.329-7.763 | 6.901-7.870 | 7.616-7.970 | 7.486-8.034 | 7.238-8.142 | 7.014-7.420 | 6.722-9.045 |
| **V** | 0.021-0.053 | 0.049-0.060 | 0.010-0.031 | 0.005-0.127 | 0.015-0.059 | 0.066-0.075 | 0.232-0.324 | 0.010-0.057 | 0.036-0.067 | 0.011-0.049 | 0.111-0.182 | 0-0.112 |
| **Ni** | 0-0.061 | 0.059-0.083 | 0.013-0.027 | 0-0.037 | 0-0.092 | 0.099-0.110 | 0.034-0.066 | 0.011-0.130 | 0.067-0.169 | 0.080-0.115 | 0.048-0.071 | 0-0.180 |
| **Zn** | 0.320-0.414 | 0 | 0.217-0.531 | 0.027-0.645 | 0.116-0.196 | 0-0.330 | 0.322-1.121 | 0-0.086 | 0-0.142 | 0-0.265 | 0.290-0.360 | 0-0.143 |
| **Co** | 0.004-0.050 | 0 | 0-0.043 | 0.004-0.050 | 0-0.038 | 0.028-0.067 | 0-0.072 | 0-0.034 | 0-0.037 | 0-0.018 | 0-0.026 | 0-0.079 |
| **Mg#** | 0.10-0.20 | 0-0.02 | 0.08-0.17 | 0.09-0.33 | 0-0.04 | 0.03-0.08 | 0.04-0.13 | 0-0.03 | 0.01-0.06 | 0.01 | 0.02-0.03 | 0-0.27 |
| **Cr#** | 0.62-0.64 | 0.97-0.99 | 0.88-0.91 | 0.75-0.91 | 0.74-0.99 | 0.91-0.93 | 0.45-0.56 | 0.99-1 | 0.92-0.99 | 0.93-1.00 | 0.91-0.93 | 0.69-1 |
| **$Fe^{3+}/R^{3+}$** | 0.01-0.05 | 0.34-0.48 | 0.08-0.22 | 0.09-0.15 | 0.15-0.58 | 0.51-0.7 | 0.03-0.25 | 0.62-0.92 | 0.77-0.93 | 0.62-0.95 | 0.27-0.42 | 0.67-0.98 |

TD: Tua Dungri, KL: Kapili, MG: Maharajgunj, All: All locations i.e., Maharajgunj, Chuka Pahar, Tua Dungri, and Kapili; Chr: Chromite, Fcmt: Ferritchromit, Chr mag: Chrome magnetite, Cr-Spl: Chrome spinel; T-I, II, III, IV, V: Type-I, II, III, IV, V; S T-I: Small type-I; R1: Inner rim, R2: Outer rim.

**Table 3: *In situ* LA-ICPMS trace elements compositional range (ppm) of komatiitic chromites from the Gorumahishani greenstone belt**

| **Location** | **Tua Dungri** | **Kapili** | **Tua Dungri** | **Tua Dungri** | **Kapili** | **Kapili** | **Maharajgunj** | **Chuka Pahar** |
|---|---|---|---|---|---|---|---|---|
| **Mineral** | **Chromite** | **Chromite** | **Ferritchromit** | **Chr mag** | **Chr mag** | **Chr mag** | **Chr mag** | **Chr mag** |
| **Type** | **T-I core** | **T-II core** | **T-I inner rim** | **T-I outer rim** | **T-II outer rim** | **T-V** | **T-V** | **T-V** |
| **Data (n)** | **4** | **2** | **2** | **4** | **2** | **4** | **6** | **5** |
| **ppm** | | | | | | | | |
| **Sc** | 2.62 - 5.40 | 3.39 - 5.68 | 0.35 - 0.53 | 0.01 - 0.96 | 0.22 - 0.92 | 0.70 - 2.47 | 0.10 - 0.32 | 0.10 - 1.20 |
| **Ti** | 534.70 - 1474.71 | 20758.92 - 36412.50 | 1097.34 - 1576.23 | 41.20 - 2369.50 | 1845.19 - 6247.98 | 2822.38 - 7855.66 | 450.83 - 2112.30 | 2899.36 |
| **V** | 863.76 - 1040.39 | 3337.90 - 7165.42 | 270.13 - 489.53 | 15.77 - 958.93 | 807.58 - 2316.46 | 1602.08 - 3102.78 | 477.59 - 1388.39 | 456.03 - 6110.31 |
| **Mn** | 6447.34 - 9946.79 | 27180.70 - 45891.24 | 3950.50 - 6453.32 | 196.29 - 11521.59 | 2107.26 - 6121.52 | 2834.59 - 6158.82 | 2761.42 - 7608.79 | 660.52 - 2307.15 |
| **Co** | 1037.17 - 1234.52 | 1744.47 - 2585.57 | 248.19 - 304.79 | 11.12 - 539.76 | 195.86 - 541.47 | 318.45 - 668.12 | 32.41 - 86.16 | 12.45 - 77.06 |
| **Ni** | 447.66 - 688.55 | 4512.85 - 10582.87 | 394.70 - 851.14 | 30.94 - 1944.89 | 1627.49 - 4705.06 | 3233.99 - 6688.57 | 847.92 - 4623.81 | 922.90 - 3328.77 |
| **Cu** | 0.09 - 2.38 | 0.23 - 3.13 | 0.04 - 0.34 | <0.03 - 2.06 | 0.17 - 0.32 | 0.03 - 0.22 | 0.03 - 0.07 | 0.03 - 0.20 |
| **Zn** | 16865.87 - 18124.18 | 11664.55 - 15757.30 | 3454.17 - 3898.71 | 196.33 - 8346.21 | 627.38 - 1746.30 | 580.29 - 938.86 | 775.48 - 3159.17 | 626.47 - 2126.8 |
| **Ga** | 10.44 - 23.48 | 49.83 - 83.7 | 1.04 - 1.11 | 0.04 - 2.25 | 6.64 - 18.88 | 12.32 - 29.39 | 0.17 - 0.52 | 0.05 - 0.12 |
| **$Cr_2O_3$** | 44.16 - 45.77 | 55.00 - 56.79 | 37.50 - 40.27 | 8.98 - 16.31 | 5.02 - 8.69 | 5.34 - 7.47 | 11.22 - 13.71 | 15.08 - 16.91 |
| **$Al_2O_3$** | 17.14 - 17.61 | 3.69 - 4.68 | 0.49 - 1.48 | 0 - 0.06 | 0.12 - 0.42 | 0.21 - 0.37 | 0.38 - 0.93 | 0.13 - 0.23 |
| **MgO** | 3.04 - 3.71 | 2.23 - 2.79 | 0.46 - 0.48 | 0.04 - 0.11 | 0.31 - 1.05 | 0.27 - 0.36 | 0.07 - 0.16 | 0.15 - 0.20 |
| **FeO** | 26.42 - 27.30 | 26.54 - 26.69 | 29.03 -29.69 | 28.97 - 30.50 | 28.76 - 29.43 | 29.45 - 29.66 | 29.57 - 29.85 | 28.27 - 28.91 |
| **$Fe_2O_3$** | 3.82 - 4.00 | 5.92 - 7.27 | 24.45 - 27.44 | 50.11 - 57.70 | 55.93 - 58.60 | 57.48 - 60.31 | 50.72 - 55.1 | 48.75 - 50.11 |
| **Mg#** | 0.17 - 0.20 | 0.13 - 0.16 | 0.02 - 0.03 | 0 - 0.01 | 0.02 - 0.06 | 0.02 | 0 - 0.01 | 0.01 |
| **$Fe^{3+}/R^{3+}$** | 0.05 | 0.08 - 0.10 | 0.35 - 0.41 | 0.74 - 0.86 | 0.85 - 0.91 | 0.87 - 0.91 | 0.77 - 0.81 | 0.73 - 0.76 |
| **Cr#** | 0.63 - 0.64 | 0.89 - 0.91 | 0.95 - 0.98 | 0.99 – 1.00 | 0.93 - 0.97 | 0.92 - 0.95 | 0.90 - 0.96 | 0.98 - 0.99 |

Chr Mag: Chrome magnetite; T-I, II, V: Type-I, II, and V; Mg#: Mg/(Mg+$Fe^{2+}$), $R^{3+}$: $Fe^{3+}$+Cr+Al, Cr#: Cr/(Cr+Al); type-I, type-II, and type-V grains are analyzed from Korea Institute of Ocean Sciences and Technologies, South Korea (29 data points)

**Table: 4: *In situ* LA-ICPMS Platinum-Group Elements (PGEs) compositional range of komatiitic chromites from the Gorumahishani greenstone belt**

| **Location** | **Tua Dungri** | **Kapili** | **Tua Dungri** | **Tua Dungri** | **Kapili** | **Kapili** | **Maharajgunj** | **Chuka Pahar** | **[a]Global data** |
|---|---|---|---|---|---|---|---|---|---|
| **Mineral** | **Chromite** | **Chromite** | **Fcmt** | **Chr mag** | **Chr mag** | **Chr mag** | **Chr mag** | **Chr mag** | **Chromite** |
| **Type** | **T-I core** | **T-II core** | **T-I R1** | **T-I R2** | **T-II R2** | **T-V** | **T-V** | **T-V** | |
| **Data (n)** | **4** | **2** | **2** | **4** | **2** | **4** | **6** | **5** | **63** |
| **ppb** | | | | | | | | | |
| **Os** | <5 - 8.8 | 8 - 8.3 | <5 | <5 | <5 | <5 - 7.3 | 15.6 - 33.4 | 19.7 - 29.8 | 5 - 54 |
| **Ir** | 7.6 - 12.4 | 8.9 - 12.3 | 8.1 - 13.4 | 5 - 11.4 | <3 | <3 - 13.5 | 17.3 - 35.7 | 12.4 - 23.8 | 14 - 101 |
| **Ru** | 127 - 163.2 | 98.1 - 123.1 | 116.9 - 197.4 | 127.5 - 206.7 | 8 - 11 | 8 - 211.5 | 86.2 - 110.9 | 72.2 - 140.6 | 87 - 336 |
| **Rh** | 28.9 - 32.6 | 4.4 - 4.9 | 29 - 38.1 | 33.6 - 44.8 | <1 | <1 - 14.4 | 2.7 - 5.7 | 2.9 - 8.9 | 7 - 95 |
| **Pt** | <2 | <12 | <2 | <2 | <12 | <12 | <12 | <12 | <3 - <5 |
| **Pd** | <14 | <14 | <14 | <14 | <14 | <14 | <14 | <14 | <1 - <4 |
| **$Rh_N/Os_N$** | 7.79 | 1.10 | | 7.83 - 19.72 | | 1.90 | 0.08 - 0.22 | 0.10 - 0.35 | 2.94 - 3.69 |
| **$Rh_N/Ir_N$** | 5.77 - 8.84 | 0.87 - 1.08 | 6.28 - 7.92 | 8.19 - 20.28 | | 2.34 | 0.17 - 0.48 | 0.40 - 0.93 | 1.10 - 2.07 |
| **$Rh_N/Ru_N$** | 0.60 - 0.77 | 0.12 - 0.13 | 0.58 - 0.74 | 0.49 - 0.97 | | 0.07 | 0.03 - 0.05 | 0.03 - 0.07 | 0.24 - 0.85 |
| **$Ru_N/Os_N$** | 12.99 | 8.27 | | 18.00 | | 29.11 | 2.86 - 5.52 | 2.43 - 6.25 | 4.36 - 12.18 |
| **$Ru_N/Ir_N$** | 7.52 - 14.75 | 7.31 - 8.10 | 10.64 - 10.84 | 8.19 - 20.28 | | 11.48 | 1.96 - 3.65 | 3.38 - 5.32 | 2.44 - 4.56 |
| **$Ir_N/Os_N$** | 0.88 | 1.02 | | 0.99 | | 1.86 | 0.84 - 1.31 | 0.53 - 0.93 | 1.79 - 2.67 |
| **$Cr_2O_3$** | 44.16 - 45.77 | 55.00 - 56.79 | 37.50 - 40.27 | 8.98 - 16.31 | 5.02 - 8.69 | 5.34 - 7.47 | 11.22 - 13.71 | 15.08 - 16.91 | 41.20 - 56.70 |
| **$Al_2O_3$** | 17.14 - 17.61 | 3.69 - 4.68 | 0.49 - 1.48 | 0 - 0.06 | 0.12 - 0.42 | 0.21 - 0.37 | 0.38 - 0.93 | 0.11 - 0.23 | 8.60 - 18.80 |
| **MgO** | 3.04 - 3.71 | 2.23 - 2.79 | 0.46 - 0.48 | 0.04 - 0.11 | 0.31 - 1.05 | 0.27 - 0.36 | 0.07 - 0.16 | 0.15 - 0.20 | 9.90 - 14.10 |
| **FeO** | 26.42 - 27.30 | 26.54 - 26.69 | 29.03 - 29.69 | 28.97 - 30.50 | 28.76 - 29.43 | 29.45 - 29.66 | 29.57 - 29.85 | 28.27 - 28.91 | 12.70 - 19.30 |
| **$Fe_2O_3$** | 3.82 - 4.00 | 5.92 - 7.27 | 24.45 - 27.44 | 50.11 - 57.70 | 55.93 - 58.60 | 57.48 - 60.31 | 50.72 - 55.10 | 48.75 - 50.11 | 4.50 - 10.70 |
| **Mg#** | 0.17 - 0.20 | 0.13 - 0.16 | 0.03 | 0 - 0.01 | 0.02 - 0.06 | 0.02 | 0 - 0.01 | 0.01 | 0.48 - 0.66 |
| **$Fe^{3+}/R^{3+}$** | 0.05 | 0.08 - 0.10 | 0.35 - 0.41 | 0.74 - 0.86 | 0.85 - 0.91 | 0.87 - 0.91 | 0.77 - 0.81 | 0.73 - 0.76 | 0.06 - 0.13 |
| **Cr#** | 0.63 - 0.64 | 0.89 - 0.91 | 0.95 - 0.98 | 0.99 – 1.00 | 0.93 - 0.97 | 0.92 - 0.95 | 0.90 - 0.96 | 0.98 - 0.99 | 0.60 - 0.82 |

Fcmt: Ferritchromit, Chr mag: Chrome magnetite; T-I, II, V: Type-I, II, V; R1: inner rim, R2: outer rim; Mg#: Mg/(Mg+Fe$^{2+}$), R$^{3+}$: Fe$^{3+}$+Cr+Al, Cr#: Cr/(Cr+Al);

[a]Global dataset for chromites from Finland komatiite and picrite, and Greenland, Kamchatka, Troodos, and Emeishan picrites (Data from Park et al. 2017)

**Table 5: Empirical partition coefficient of trace elements ($D^{\text{Cr-spinel-silicate melt}}$)**

| Sample | MIC/16/39 | | | SHB/19-12/82 | |
|---|---|---|---|---|---|
| Type | T-I C | T-I C | T-I C | T-II C | T-II C |
| Location | Tua Dungri | Tua Dungri | Tua Dungri | Kapili | Kapili |
| $D_{Sc}$ | 0.37 | 0.45 | 0.38 | 0.26 | 0.15 |
| $D_{Ti}$ | 0.13 | 0.12 | 0.12 | 12.28 | 6.77 |
| $D_{V}$ | 14.21 | 14.34 | 14.08 | 109.52 | 37.21 |
| $D_{Mn}$ | 2.69 | 2.57 | 2.51 | 32.65 | 17.81 |
| $D_{Co}$ | 12.10 | 11.99 | 11.58 | 37.66 | 23.52 |
| $D_{Ni}$ | 0.24 | 0.28 | 0.26 | 12.13 | 4.95 |
| $D_{Ga}$ | 8.46 | 11.04 | 8.44 | 20.87 | 11.78 |

T-I C: Type-I core, T-II C: Type-II core

**Table 6: Empirical partition coefficient of IPGEs and Rh ($D^{\text{Cr-spinel-silicate melt}}$)**

| Sample | MIC/16/39 | | | | SHB/19-12/82 | |
|---|---|---|---|---|---|---|
| Type | T-I C | T-I C | T-I C | T-I C | T-II C | T-II C |
| Location | Tua Dungri | Tua Dungri | Tua Dungri | Tua Dungri | Kapili | Kapili |
| $D_{Ru}$ | 67.86 | 51.73 | 49.79 | 51.74 | 35.51 | 45.43 |
| $D_{Rh}$ | 36.94 | 36.66 | 36.71 | 32.21 | 4.40 | 4.94 |
| $D_{Os}$ | | 4.45 | | | 8.18 | 8.45 |
| $D_{Ir}$ | 2.72 | 2.73 | 4.18 | 2.54 | 2.23 | 3.10 |

T-I C: Type-I core, T-II C: Type-II core

# Fractionation of trace and platinum-group elements during metamorphism of komatiitic chromites from the early Archean Gorumahishani greenstone belt, Singhbhum Craton (eastern India)

**Ratul Banerjee[a], Sisir K. Mondal[a]*, Laurie Reisberg[b], Jung-Woo Park[c]**

[a] Department of Geological Sciences, Jadavpur University, 188, Raja S.C. Mullik Road, Kolkata-700032, India
[b] Centre de Recherches Pétrographiques et Géochimiques, UMR 7358 Université de Lorraine - CNRS, France
[c] School of Earth and Environmental Sciences, Seoul National University, Seoul, 08826, South Korea

*Corresponding Author:
eMail: smondal@amnh.org
Phone: 0091-33-24572730

## Detailed information on the geological background of the Singhbhum craton and analytical methods

## Geological background

The Singhbhum Craton in eastern India is bounded by the Singhbhum mobile belt to the north, the Satpura metamorphic belt to the northwest, the granulite facies Eastern Ghat mobile belt in the southeast with a tectonic contact marked by the Sukinda thrust, and the alluvium of the Bengal basin to the east (Saha 1994) (**Fig. 1a**). The Archean granitic-gneissic nucleus of the craton is surrounded by the greenschist to amphibolites facies volcano-sedimentary supracrustal rocks of the greenstone belts (**Fig. 1a**). Among the supracrustal rocks, the Older Metamorphic Group (OMG: 3.55 Ga zircon age, Mishra et al. 1999) shows the metamorphic events clustering at 3.4, 3.35, and 3.2 Ga (Goswami et al. 1995; Mishra et al. 1999; Upadhyay et al. 2014, 2019). The OMG is consisting of pelitic schist, arenite, para-amphibolite, and ortho-amphibolite (e.g. Saha 1994) that were intruded by Older Tonalite-Trondhjemite-Granodiorite (OMTG) rocks consist of thin compositionally layered, tonalitic to granodioritic gneisses along with granites (e.g. Saha 1994). Voluminous granitic rocks constitute the Singhbhum Granite Batholithic Complex (SGBC) with their emplacement in three successive phases (I, II, and III; Saha 1994) along with the OMTG rocks at 3.45 - 3.44 Ga and 3.35 - 3.32 Ga (Upadhyay et al. 2014) (**Fig. 1a**). Chaudhuri et al. (2018) reported a U-Pb age of 4.24 - 4.03 Ga of xenocrystic zircons from the OMTG rocks. The volcano-sedimentary rocks of the greenstone belts belonging to the Iron Ore Group (IOG) supracrustal sequences are distributed in the Gorumahisani-Badampahar, Noamundi-Jamda-Koira, and Tomka-Daitari belts (e.g. Acharyya 1993; Mondal 2009) (**Fig. 1a**). Komatiites and komatiitic basalts are the main volcanic sequences that are intercalated with the sedimentary sequences of phyllite, tuffaceous shale, banded hematite jasper with iron ore, quartzites, and dolomite (Sahu and Mukherjee 2001; Chaudhuri et al. 2015, 2017; Yadav et al. 2015, 2017; Mondal et al. 2019) (**Fig. 1b-e**). Mukhopadhyay et al. (2008) have determined a U-Pb zircon age of 3.5 Ga from the dacitic lavas of the Tomka-Daitari belt and Basu et al. (2008) have determined a U-Pb zircon age of 3.4 Ga from a tuff layer within the Noamundi-Jamda-Koira belt. Adhikari et al. (2021a) have determined the Sm-Nd isochron age of ~3.6 Ga for the metabasaltic rocks of the Tomka-Daitari greenstone belt. Mesoarchean to late Archean Dhanjori-Jagannathpur-Malangtoli-Simlipal volcano-sedimentary belts surround the rocks of the older greenstone belts (OMG and IOG) and granite-gneiss complexes of the OMTG and the SGBC (e.g. Mondal 2009) (**Fig. 1a**). Adhikari et al. (2021b) have determined the Sm-Nd isochron age of 2799 ± 67 Ma for the basaltic rocks from the Jagannathpur-Malangtoli belt. Mesoarchean to late Archean Nuasahi-Sukinda-Mayurbhanj complexes with chromite, Ni-Cu-sulfides, PGE and Ti-V-magnetite deposits are the major ultramafic-mafic plutonic suites in the craton (e.g. Mondal et al. 2007; Manikyamba et al. 2020; Bhattacharjee and Mondal 2021; Mondal et al. 2021) (**Fig. 1a)**. The mafic dyke systems of Mesoarchean to late Proterozoic ages are exposed within the SGBC of the craton (e.g. Mazumder and Chaudhuri 2019; Srivastava et al. 2019; Dey and Mondal 2021) (**Fig. 1b**).

## Analytical methods

Back-scattered electron (BSE) imaging and microanalysis of the mineral phases (oxides and silicates) of a total of 8 representative samples were carried out using a CAMECA SXFive EPMA instrument at DST-SERB National Facility, Department of Geology, Banaras Hindu University (India). Another 14 samples were analyzed by 4-WDX CAMECA SX-100 EPMA at the Department of Geology and Geophysics, Indian Institute of Technology, Kharagpur (India). The CAMECA SXFive EPMA was operated by SXFive Software at a voltage of 15 kV and beam current of 10 nA whereas the 4-WDX CAMECA SX-100 EPMA was controlled by a beam current of 15 nA and acceleration voltage of 20 kV. Natural mineral standards fluorite, apatite, albite, halite, periclase, peridote, corundum, wollastonite, orthoclase, rutile, chromite, rhodonite, celestite, barite, hematite, crocoite, pyrite, and synthetic $Ag_2Te$, InAs, InSb, Ni, Co, Cu, Zn metal supplied by CAMECA-AMETEK were used for routine calibration and quantification during analysis. Routine calibration, acquisition, quantification, and data processing were carried out using SxSAB version 6.1 and SX-Results software of CAMECA. ZAF matrix corrections were performed by the CAMECA-supplied PAPSIL software. Representative data of mineral compositions are presented in **Table 1** (silicates and carbonates), and **Table 2** (oxides), and the complete data sets are also available in **Appendix 03: Table S1-S2**.

Trace element and PGE contents in chromite, ferritchromit, and chrome-magnetite were also measured by an LA-ICP-MS system for selected elements (Sc, Ti, V, Mn, Co, Ni, Cu, Zn, Ga, Os, Ir, Ru, Rh, Pt, Pd) consisting of a New Wave 193 nm ArF excimer laser and an Agilent 7800 quadrupole ICP-MS at Korea Institute of Ocean Sciences and Technologies, South Korea. The ablation conditions were a 10 Hz repetition rate, an 80-100 µm beam size and ~ 5 J/cm$^2$ energy density. The NIST 610 glass was used as a primary standard and Al contents measured by a microprobe was an internal standard element for calculating trace element. Representative data of trace elements from chromite are presented in **Table 3** and the complete data set is available in **Appendix 03: Table S3.** The sulfide reference material UQAC-FeS-1 was used as a primary standard and Fe contents as an internal standard element for platinum-group elements (PGE). The data reduction was conducted by Iolite software (Paton et al. 2011). The isobaric interference by metal oxides (MO+) and metal argides (MAr+) were checked by analyses of pure Cu metal (C-430, Fisher Scientific Company) and PGE-free synthetic Ni-sulphide. The expected isobaric interferences are ~1 ppb Ru per 1000 ppm Ni and ~7 ppb Rh per 1000 ppm Cu in Cr-spinels, which result in negligible isobaric interferences of $^{61}Ni^{40}Ar$ + and $^{63}Cu^{40}Ar$ + on $^{101}Ru$ and $^{103}Rh$ (<2 %) for most samples. Any micro inclusions, identified as spikes in time-resolved spectra data, were excluded when calculating the concentrations. Multiple analyses (n=7) of Cr-spinels from Kamchatka picrite (Ty24) were performed using the UQAC-FeS-1 reference material to externally monitor the quality of the PGE data. Our results are consistent with the values reported in Park et al. (2017) within 1 standard deviation as reported in **Appendix 03: Table S4**. Representative data of PGE are also presented in **Table 4**.

For whole-rock analysis, samples were cleaned, crushed, and pulverized to a 200-mesh size in the Department of Geological Sciences, at Jadavpur University. The crushing and pulverization work was carried out by single bowl RO milling systems (Model MBM 07, Insmart systems). The grinding was carried out by high energy frequent impact of agate (99.9% $SiO_2$, 7.0Mohs hardness, and 2.65 g/cc density) balls. At 600 rpm, 100 g of the sample was crushed by the machine in 45 min. Wole-rock major, trace, and platinum-group elements alongside C and S were conducted from Intertek Genalysis, Perth, Western Australia. For major elements, approximately 0.7g was catch weighed into a platinum crucible and this was mixed with a pre-weighed amount of flux which was comprised of a mixture of lithium tetraborate and lithium metaborate. An oxidant was added and the sample was fused to produce a homogeneous melt which was cast into a platinum mould to produce a fusion disk. The fusion disk was analysed on a Panalytical Axios sequential wavelength-dispersive X-ray fluorescence spectrometer. Calibration was affected by standard glass beads of known composition. Corrections were made for the catch weights, instrumental drift, line overlaps and inter-element enhancement/absorption matrix effects as well as moisture (done by the TGA). Standard OREAS 24b was used as reference material for this case. LOI was analyzed using a TGA or thermo gravimetric analyzer. The instrument weighed the inert crucible. Approximately 1 g of sample was added to the crucible. The instrument weighed the crucible and sample. The mass of the sample taken was determined by difference. The sample was then heated to constant mass at 105°C and weighed. The mass lost as a fraction of the mass taken was the moisture. The sample was then heated to constant mass at 1000°C and weighed. The mass lost as a fraction of the dry mass was the loss on ignition or LOI. For trace elements, the pulped samples are catch weighed at 0.20g ± 0.02g into a Teflon tube. The tube was placed in a rack and the digesting acids are added sequentially with nitric acid pre-oxidation of sulphides. The rack was placed on a “hot block” which provides even heat to decompose the sample and ensure to ensure maximum dissolution. The perchloric ($HClO_4$) acid was evaporated and the residue leached by boiling in HCl. The solution was transferred to a polystyrene tube where it was volumed and mixed. A further dilution of the digest solution was required before reading on the Agilent 7900 ICPMS with collision cell technology. Calibration was affected using solution standards of known concertation. Standard OREAS 45h is used for trace elements analysis. For platinum-group elements (PGE) analysis the pulped samples were catch weighed at 25grams and mixed with a flux and fired in a furnace. When fired, the flux sample mixed forms a nickel sulphide matte and an immiscible slag which separate owing to density differences. The precious metals were collected in the nickel sulphide matte (button). The button was separated from the slag, weighed and pulverized. A portion of the pulverized button was catch weighed and dissolved in boiling HCl. The addition of various reagents to the boiling HCl solution and careful observation of the dissolution process ensures that the platinum group elements and gold were quantitatively recovered by filtration as insoluble residues. These residues were dissolved in aqua regia. The solution was diluted and read on an ICP mass spectrometer with collision cell technology to remove polyatomic interferences, especially first-row transition element argide species. Internal standards are used to correct for drift and plasma fluctuations. The results are corrected for the various catch weights and the button weight by the LIMS system. Standard OREAS 13b was used for PGE+Au analysis. Carbon (C) and Sulfur (S) analysis was performed in an Eltra CS800 Carbon–Sulphur Analyser. The pulped sample was weighed out and placed in a ceramic crucible. An accelerant was added to act as a flux and improve fluidity and oxidation of the carbon and sulphur. Heating was accomplished in a high-frequency induction furnace as this provides both speed and accuracy. Any sulphur or carbon was converted to gaseous oxides. These gases absorb infrared radiation at specific wavelengths which were proportional to the concentration of the C or S in the sample. Any water in the sample was removed by passing the gases produced through magnesium perchlorate as water interferes with the analysis. Calibration was affected by the standard of known C and S concentration. Standard OREAS 600b was used here as reference material. The complete whole-rock data set is presented in **Appendix 03: Table S5**.

**References**

Acharyya SK (1993) Greenstones from Singhbhum Craton, their Archaean character, oceanic crustal affinity and tectonics. Proc Natl Acad Sci India 63:211-222

Adhikari A, Mukherjee S, Vadlamani R (2021a) A plume-mantle interaction model for the petrogenesis of komatiite-komatiitic basalt-basalt-basaltic andesite volcanism from the Paleoarchean (3.57-3.31 Ga) Iron Ore Group greenstone belts, Singhbhum craton, India: Constraints from trace element geochemistry and Sm-Nd geochronology. Lithos 398-399:106315

Adhikari A, Nandi A, Mukherjee S, Vadlamani R (2021b) Petrogenesis of Neoarchean (2.80-

2.75 Ga) Jagannathpur volcanics and the Ghatgaon and Keshargaria dyke swarms, Singhbhum craton, eastern India: Geochemical, Sr-Nd isotopic and Sm-Nd geochronologic constraints for interaction of enriched-DMM derived magma with metasomatised subcontinental lithospheric mantle. Lithos 400-401:106373

Basu AR, Bandyopadhyay PK, Chakrabarti R, Zou H (2008) Late 3.4 Ga Algoma-type BIF in the Eastern Indian Craton. Geochim et Cosmochim Acta 72:A59

Bhattacharjee C, Mondal SK (2021) Geochemistry of Fe-Ti oxide and sulfide minerals in gabbroic rocks and magnetitite of the Archean Mayurbhanj mafic complex (eastern India): Magma fractionation, thermometry and oxygen fugacity of re-equilibration, and implications for Ni-Cu mineralization. Ore Geol Rev 131:104005

Chaudhuri T, Mazumder R, Arima M (2015) Petrography and geochemistry of Mesoarchaean komatiites from the eastern Iron Ore belt, Singhbhum craton, India, and its similarity with ‘Barberton type komatiite’. J Afr Earth Sci 101:135-147

Chaudhuri T, Satish-Kumar M, Mazumder R, Biswas S (2017) Geochemistry and Sm- Nd isotopic characteristics of the Paleoarchean Komatiites from Singhbhum Craton, Eastern India and their implications. Precambrian Res 298:385-402

Chaudhuri T, Wan YS, Mazumder R, Ma MZ, Liu DY (2018) Evidence of enriched, Hadean Mantle Reservoir from 4.2–4.0 Ga zircon xenocrysts from Paleoarchean TTGs of the Singhbhum Craton, Eastern India. Sci Rep 8:7069

Dey A, Mondal SK (2021) Origin of Fe-Ni-Cu sulfides in the 1.77Ga mafic dyke from Satkosia area, Singhbhum Craton (eastern India). Virtual Goldschmidt 2021

Goswami JN, Misra S, Wiedenbeck M, Ray SL, Saha AK (1995) 3.55 Ga old zircon from Singhbhum-Orissa iron ore craton, eastern India. Curr Sci 69:1008-1011

Manikyamba C, Pahari A, Santosh M, Ray J, Sindhuja CS, Subramanyam KSV, Singh MR (2020) Mesoarchean gabbro-anorthosite complex from Singhbhum Craton, India. Lithos 366-367:105541

Mazumder R, Chaudhuri T (2019) Precambrian mafic dyke swarms in the Singhbhum craton (eastern India) and their links with dyke swarms of the eastern Dharwar craton (southern India)-Discussion. Precambrian Res 329:18-22

Misra S, Deomurari MP, Wiedenbeck M, Goswami JN, Ray S, Saha AK (1999) $^{207}$Pb/$^{206}$Pb zircon ages and the evolution of the Singhbhum Craton, eastern India: an ion microprobe study. Precambrian Res 93:139-151

Mondal SK, Frei R, Ripley EM (2007) Os isotope systematics of Mesoarchean chromitite-PGE deposits in the Singhbhum craton (India): implications for the evolution of lithospheric mantle. Chem Geol 244:391-408

Mondal SK (2009) Chromite and PGE deposits of Mesoarchaean ultramafic-mafic suites within the greenstone belts of the Singhbhum craton, India: implications for mantle heterogeneity and tectonic setting. J Geol Soc India 73:36-51

Mondal SK, Das E, Banerjee R, Reisberg L (2019) Trace Element in Chromites of Komatiites from the Archean Gorumahisani Greenstone Belt, Singhbhum Craton (India). Goldschmidt 2019, Barcelona (Spain)

Mondal SK, Bhattacharjee C, Reisberg L (2021) 3.2-3.0 Ga Sm-Nd age of gabbro-anorthositic rocks from the Nuasahi and Mayurbhanj Complexes (eastern India): Major mafic magmatic event in the Singhbhum Craton and associated Ni-Cu-(PGE) sulphide mineralization. Virtual Goldschmidt 2021

Mukhopadhyay J, Beukes NJ, Armstrong RA, Zimmermann U, Ghosh G, Medda RA (2008) Dating the oldest Greenstone in India, a 3.51-Ga precise U–Pb SHRIMP zircon age for

Dacitic Lava of the Southern Iron Ore Group, Singhbhum Craton. J Geol 116:449-461

Park J-W, Kamenetsky V, Campbell I, Park G, Hanski E, Pushkarev E (2017) Empirical constraints on partitioning of platinum group elements between Cr-spinel and primitive terrestrial magmas. Geochim Cosmochim Acta 216:393-416

Paton C, Hellstrom J, Paul B et al (2011) Iolite: freeware for the visualisation and processing of mass spectrometric data. J Anal At Spectrom 26(12):2508

Saha AK (1994) Crustal evolution of Singhbhum-North Orissa, eastern India. Geol Soc India 27:1-341

Sahu N K, Mukherjee MM (2001) Spinifex textured komatiite from Badampahar-Gorumahisani schist belt, Mayurbhanj District, Orissa. J Geol Soc India 57:529-534

Srivastava RK, Söderlund U, Ernst RE, Mondal SK, Samal AK (2019) Precambrian mafic dyke swarms in the Singhbhum craton (eastern India) and their links with dyke swarms of the eastern Dharwar craton (southern India). Precambrian Res 329:5-17

Upadhdyay D, Chattopadhyay S, Kooijman E, Mezger K, Berndt J (2014) Magmatic and metamorphic history of Paleoarchean tonalite-trondhjemite-granodiorite (TTG) suite from the Singhbhum craton, eastern India. Precambrian Res 252:180-190

Upadhyay D, Chattopadhyay S, Mezger K (2019) Formation of Paleoarchean-Mesoarchean Na-rich (TTG) and K-rich granitoid crust of the Singhbhum craton, eastern India: constraints from major and trace element geochemistry and Sr-Nd-Hf isotope composition. Precambrian Res 327:255-272

Yadav PK, Pradhan UK, Mukherjee A, Sar RN, Sahoo P, Das M (2015) Basic characterization of Kapili komatiite from Badampahar-Gorumahishani schist belt, Singhbhum Craton, Odisha, India. Indian J Geosci 69:1-12

Yadav PK, Das M (2017) Geochemistry of Kapili komatiite from Badampahar-

Gorumahisani greenstone belt, Singhbhum craton, India and its resemblance with 'Barberton Komatiite'. Int j res Anal Rev 4:495-507

# Fractionation of trace and platinum-group elements during metamorphism of komatiitic chromites from the early Archean Gorumahishani greenstone belt, Singhbhum Craton (eastern India)

**Ratul Banerjee[a], Sisir K. Mondal[a]*, Laurie Reisberg[b], Jung-Woo Park[c]**

[a] Department of Geological Sciences, Jadavpur University, 188, Raja S.C. Mullik Road, Kolkata-700032, India

[b] Centre de Recherches Pétrographiques et Géochimiques, UMR 7358 Université de Lorraine - CNRS, France

[c] School of Earth and Environmental Sciences, Seoul National University, Seoul, 08826, South Korea

*Corresponding Author:
eMail: smondal@amnh.org
Phone: 0091-33-24572730

**Supplementary online material for figures**

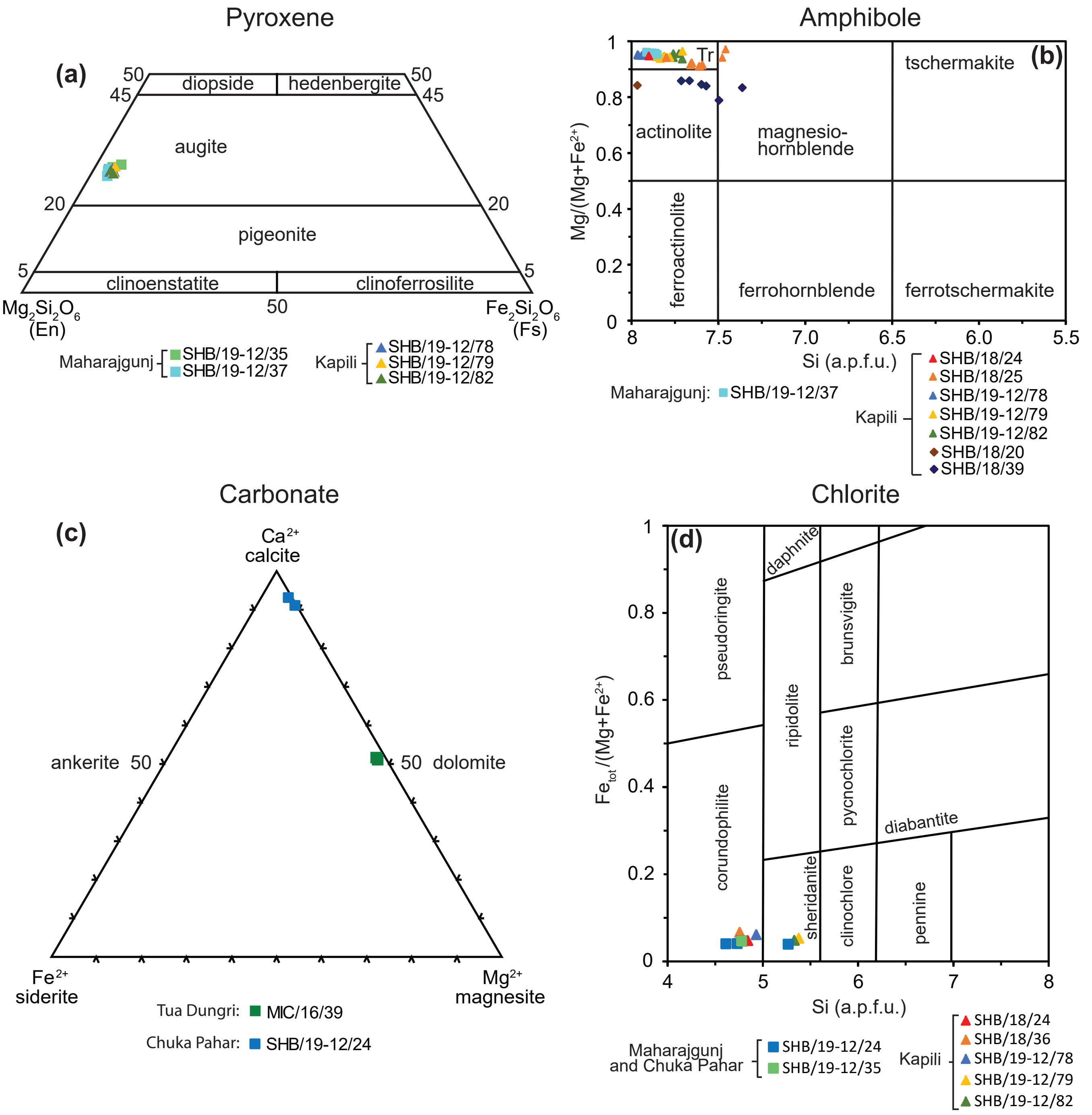

**Fig. S1** (***a***) Classification of pyroxene (after Morimoto 1988), (***b***) amphibole (after Leake et al. 1997), (***c***) carbonate, and (***d***) chlorite (after Hey 1954) from the komatiitic suite of rocks from the Gorumahishani greenstone belt.

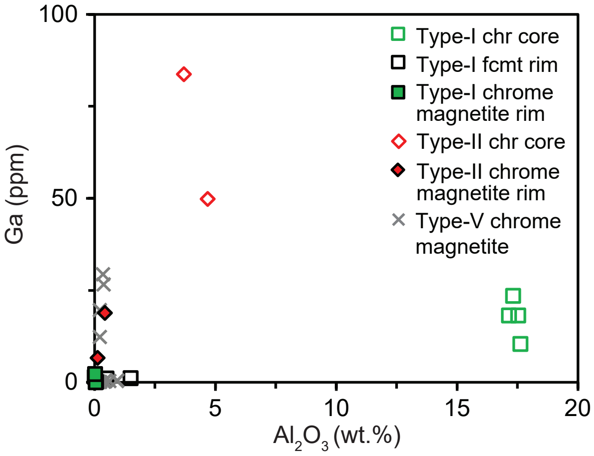

**Fig. S2** Compositional variations of the type-I, type-II, and type-V chromite grains: $Al_2O_3$ vs Ga plot.

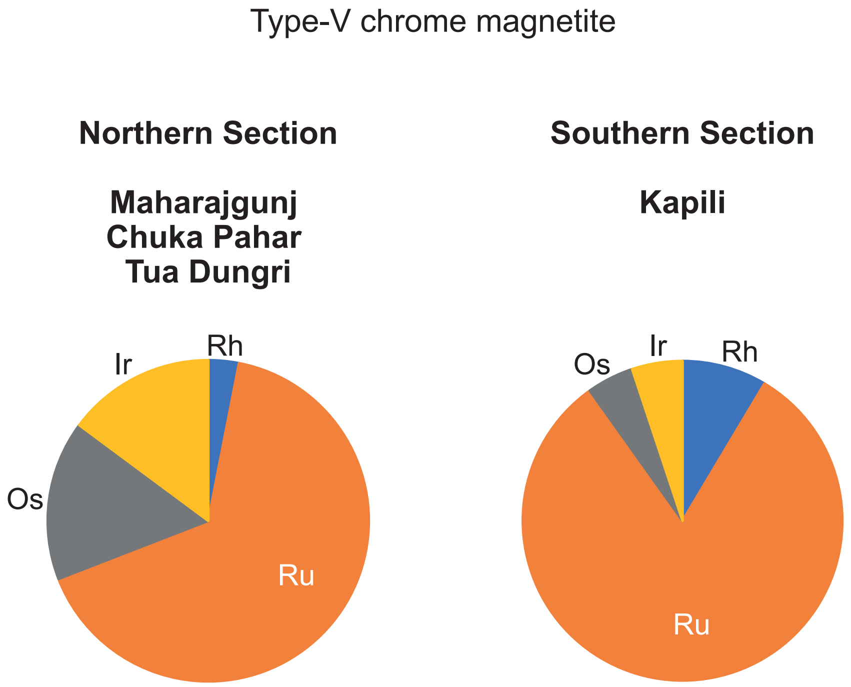

**Fig. S3** Variation in platinum-group elements concentration (in ppb) of the type-V chrome magnetite grains from the northern and southern part of the Gorumahisani greenstone belt.

## References

Frost BR (1991) Introduction to oxygen fugacity and its petrologic importance. Rev Mineral Geochem 25(1):1-9

Hey MH (1954) A new review of the chlorites. Mineral Mag 30:217-292

Leake BE, Woolley AR, Arps CES, Birch WD, Gilbert MC, Grice JD, Hawthorne FC, Kato A, Kisch HJ, Krivovichev VG, Linthout K, Laird J, Mandarino JA, Maresch WV, Nickel EH, Rock NMS, Schumacher JC, Smith DC, Stephenson NCN, Ungaretti L, Whittaker EJW, Youzhi G (1997) Nomenclature of amphiboles: Report of the Subcommittee on Amphiboles of the International Mineralogical Association, Commission on New Minerals and Mineral Names. Am Min 82:1019-1037

Morimoto N (1988) Nomenclature of pyroxenes. Mineral Petrol 39:55-76